GENERATION OF HIGH-ENERGY NEUTRAL RADIATION IN FLARE LOOPS

II. *Monte Carlo Simulation and Comparison with Observations*

V. G. GUEGLENKO, G. E. KOCHAROV, G. A. KOVALTSOV

A. F. Ioffe Physico-Technical Institute, Leningrad, 194021, U.S.S.R.

L. G. KOCHAROV

Leningrad Polytechnical Institute, Leningrad, 195251, U.S.S.R.

and

N. Z. MANDZHAVIDZE

Institute of Geophysics, Tbilisi, 380093, U.S.S.R.

(Received in revised form 25 April, 1989)

Abstract. We consider the generation of high-energy neutron and π^0-decay γ-quanta inside magnetic loops on the Sun. Using Monte Carlo simulations we investigate the influence of pitch-angle diffusion upon the characteristics of secondary emission. We consider various cases of diffusion on exterior MHD-turbulence as well as on Alfvén waves generated by accelerated particles through the cyclotron instability. We compare the calculated results to SMM flare observations and show that the observational data on the 3 June, 1982 flare do not contradict the assumption of the impulsive phase acceleration of all the protons, given that the energy spectrum of the accelerated particles is an energy power law.

1. Introduction

Since the problem was first studied, the high-energy neutral radiation from solar flares has been considered under the assumption that there is an isotropic generation of secondary products (see Lingenfelter *et al.*, 1965; Lingenfelter and Ramaty, 1967). Neither the inhomogeneity of the solar atmosphere nor the influence of the magnetic field on the motion of accelerated particles have been taken into account. G. Kocharov and Mandzhavidze (1983, 1984) and Hua and Lingenfelter (1987a, b) calculated the neutron generation caused by focused proton beams propagating through an inhomogeneous atmosphere in different directions. In their calculations, the influence of the magnetic field was omitted. In order to consider the bremsstrahlung of relativistic electrons Dermer and Ramaty (1986) simulated the influence of the magnetic field by the introduction of an *ad hoc* distribution function of accelerated electrons. A direct analytical calculation, including the magnetic field as well as the atmospheric inhomogeneity, is presented in Paper I (L. Kocharov and Kovaltsov, 1989, see also references therein). That paper proves the statement that inasmuch as accelerated particles move inside some kind of magnetic arch even when the initial distribution of accelerated particles is isotropic, the secondary emission will be anisotropic. We should mention that the results obtained in Paper I do not include the scattering of primary and secondary

Solar Physics **125:** 91–123, 1990.

particles. When considering the secondary neutrons and π^0-decay γ-quanta, it is necessary to take into account collisions with ambient particles. Besides, when turbulent magnetic fields are present, the effect of pitch-angle scattering of primary particles on those fields becomes significant. It seems convenient to apply the Monte Carlo procedure to the problem.

We make the same assumptions as in Paper I, namely that primary particles undergo acceleration at the top of the arch and generate secondary products as they move between two magnetic mirrors at the foots of the arch or precipitate into dense regions of the atmosphere. We assume that under the transition layer the density of matter rises exponentially ($n = n_0 \exp(-z/h_A)$) while the magnetic field rises linearly ($B = B_c(1 - z/h_\mu)$). The magnetic field strength and density in the corona are considered to be constant, B_c and n_c. Inside the photosphere ($-z > Z_{ph} = 2 \times 10^8$ cm) the magnetic field is also supposed to be constant, B_{ph}, i.e., the mirror ratio $\rho = B_{ph}/B_c = 1 + Z_{ph}/h_\mu$. The scale of the atmospheric homogeneity is $h_A = 2 \times 10^7$ cm; the ratio h_μ/h_A, determining the emission directivity (see Equation (14) in Paper I), varies. The particle deceleration rate, as well as the secondary emission decay time, depend upon the matter density n_0 under the transition layer. 10^{11}–10^{13} cm^{-3} are typical values for the number density in impulsive high-energy flares (de Jager, 1987). So the basic parameters are $n_0 = 10^{12}$ cm^{-3}, $n_c = 10^{11}$ cm^{-3}, $h_\mu/h_A = 4$, arch radius $R_A = 10^9$ cm (arch length is πR_A), and the relative ^{4}He abundance in solar matter and in the accelerated particles is $n_{\mathrm{He}}/n_{\mathrm{H}} = 0.07$. The initial spectrum of accelerated protons is chosen to be a power law in energy ($\mathrm{d}N/\mathrm{d}E = AE^{-S_p}$), the initial angular distribution being isotropic. Reading Sections 2 and 3 one should note that accelerated particles are supposed to be injected at the top of the arch instantaneously at $t = 0$. Meanwhile, the consideration of flare events that actually occurred (Section 5) requires special injection functions drawn from the observational data.

2. High-Energy Neutron and π^0-Decay Gamma-Radiation

The particles responsible for the production of high-energy (> 50 MeV) neutrons and γ-radiation from neutral pion decay have energy in the range of hundreds of MeV to several GeV. For these particles, together with the ionization losses, nuclear collisions become important causing abrupt changes in particle energy and direction. Considering the propagation of neutral radiation through the solar atmosphere, account must be taken of the elastic and inelastic collisions of neutrons with ambient hydrogen as well as Compton scattering and pair production effects for γ-rays. Therefore, to calculate the time-dependent production and angular and energy distributions of escaping neutrons and γ-quanta we have used the Monte Carlo simulation technique. Details of calculations are presented in Appendix II.

The main sources of > 50 MeV neutrons are the pp, $p\alpha$, and αp reactions, while the two former are also most important for π^0-generation. We obtained angular and energy distributions of pp-reaction products using the biparametrical polynomial approxima-

tion presented by Barashenkov *et al.* (1969). We re-examined the inclusive cross-sections as well as the angular and energy distributions of secondaries in $p\alpha$ and $\alpha\alpha$ reactions. The re-examined cross-sections are given in Appendix I. The principal difference from the analyses by other authors (Hua and Lingenfelter, 1987a, b and Murphy, Dermer, and Ramaty, 1987) lies in the use of the double differential cross-sections $d^2\sigma/dE_n d\Omega_k$ instead of the 4π average cross-section $d\sigma/dE_n$ which is essential for the calculation of neutron anisotropy. Also in these papers the neutron energies in the $\alpha\alpha$ reaction were overestimated as the uniform energy distribution was extended up to a maximal value. For this reason the energy spectra resulting from our calculations (Figure 1) are a little steeper than those obtained by Hua and Lingenfelter (1987a, b)

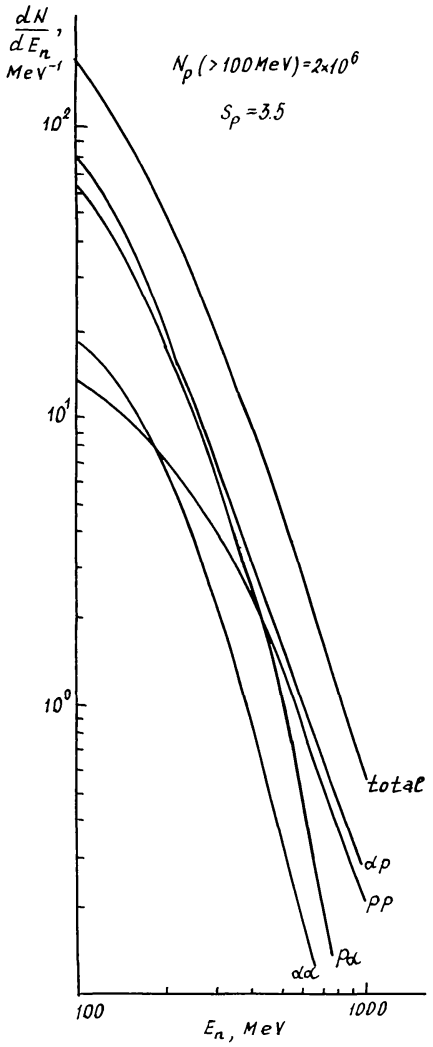

Fig. 1. Neutron production spectra in different reactions.

and Murphy, Dermer, and Ramaty (1987). The neutron production in various reactions for the > 50 MeV and > 500 MeV neutron energy bands is shown in Figure 2. The neutron birth threshold (≈ 25 MeV n^{-1}) is much less than that of the *pp* reaction (292 MeV). Therefore, most of the not-very-high-energy neutrons are produced in the

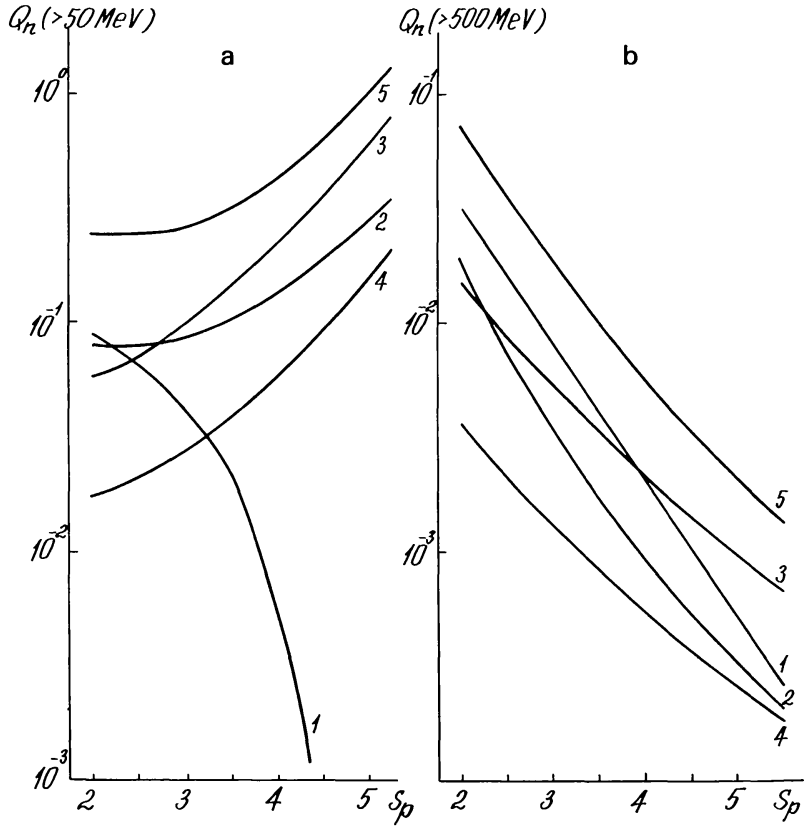

Fig. 2. Thick-target total and partial neutron production for neutron energy > 50 MeV (a) and > 500 MeV (b). The primary ion energy spectra are power law: E^{-S_p}, N_p (> 300 MeV) = 1. (1) pp, (2) $p\alpha$, (3) αp, (4) $\alpha\alpha$, (5) total.

$p\alpha$ and αp reactions (if the energy spectra of the accelerated particles are a power law). pp reaction becomes rather prominent for the generation of high-energy neutrons.

The total π^0 generation rate in a thick-target model obtained for various values of the ion spectrum index S_p is, on average, 1.1–1.2 times lower than that presented by Ramaty and Murphy (1984). This could be due to a difference in the cross-sections of inclusive pion production in the $p\alpha$ interaction.

The $p\alpha$ and αp channels yield almost 40% of the total π^0 generation rate, slightly varying with the power law spectral index S_p. The calculations made it clear that protons that are rescattered in nuclear collisions yield no more than 20% of the total π^0 production rate.

As was shown in Paper I, all the accelerated particles moving inside the arch may be separated into three populations which differ by pitch-angle cosine $\mu_0 = \cos\vartheta_0$ at the top of the arch: (1) particles with small pitch-angles $\mu_0 > \mu_1$, i.e., those which do not return to the corona because they belong to the loss cone ($\mu_0 > \mu_l = \sqrt{1 - \rho^{-1}}$) or because they decelerate rapidly in the chromosphere ($\mu_1 < \mu_0 < \mu_l$); (ii) trapped ions returning to the corona, but decelerating while in the chromosphere ($\mu_1 > \mu_0 > \mu_2$); (iii) trapped particles tending to decelerate in the corona ($\mu_0 < \mu_2$). The time dependence of the rate of neutron generation ($E_n > 50$ MeV), which is shown in Figure 3(a), is determined by the subsequent deceleration of primary particles with different μ_0. The

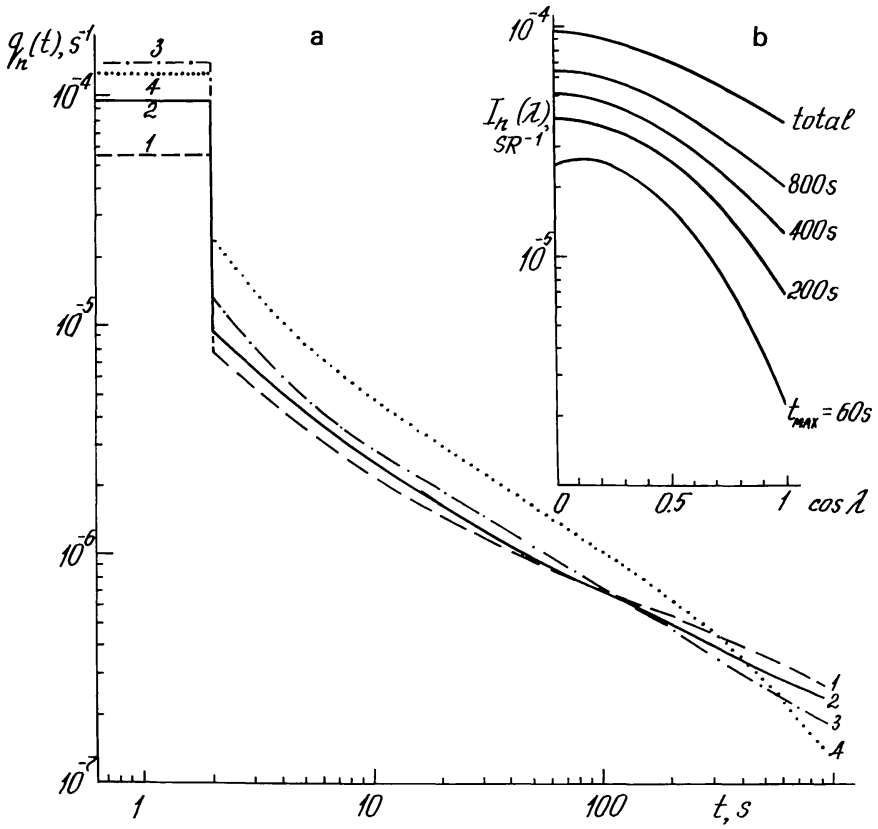

Fig. 3. (a) Generation rate of >50 MeV neutrons. $R_A = 10^9$ cm, $n_c = 10^{11}$ cm^{-3}, $h_A = 2 \times 10^7$ cm. (1) $h_\mu/h_A = 2$, $n_0 = 10^{12}$ cm^{-3}. (2) $h_\mu/h_A = 4$, $n_0 = 10^{12}$ cm^{-3}. (3) $h_\mu/h_A = 8$, $n_0 = 10^{12}$ cm^{-3}. (4) $h_\mu/h_A = 4$, $n_0 = 10^{13}$ cm^{-3}. (b) Angular distribution of escaping neutrons (>50 MeV) integrated over time (from $t = 0$ to $t = t_{max}$). λ is the angular distance from the flare site to the disk center. Parameters are the same as for curve 2 in Figure 3(a). In both figures the primary ion energy spectra are power law: $S_p = 3.5$, N_p (>30 MeV) $= 1$.

impulsive part in Figure 3(a) ($t < 2$ s) is mainly determined by the first population of protons ($\mu_0 > \mu_1$). Later, most of the emission is produced by the second population. Here the $q_n(t)$-dependence proves to be close to a power law, in agreement with the results obtained in Paper I. The radiation from particles of the third population ($\mu_0 < \mu_2$) tends to dominate at later periods not depicted in Figure 3(a). Provided one is not interested in the far tail of the emission, we may draw the statement that the generation rate $q_n(t)$ is determined by the medium parameters below the transition layer, namely n_0 and h_μ. Meanwhile its dependence upon the coronal plasma density n_c, as well as on arch radius R_A, is rather weak. As seen in Figure 3(a), an increase in the h_μ/h_A ratio would bring about an increase in the impulsive component of the burst and also the steepening of its tail. The reason for that lies in the fact that as the magnetic field gradient in the chromosphere decreases, particles tend to penetrate more deeply inside the solar atmosphere and to slow down more rapidly. A plasma density increase (at fixed h_μ/h_A) would have similar consequences (curve 4 in Figure 3(a)). Small pitch-angled particles ($\mu_0 > \mu_1$) which produce emission that dominates at the beginning traverse most of the column density, moving downwards inside the solar atmosphere. Particles

of the second population slow down near the mirror point, while moving almost parallel to the solar surface. Keeping in mind that secondary neutrons are produced mainly along the direction of the velocity of primary protons, one can conclude that neutron fluxes generated by particles of the first two populations tend to increase as the heliolongitude becomes higher. That effect, illustrated in Figure 3(b), becomes less significant at later stages of the flare. $I_n(\lambda)$ is the neutron radiation intensity integrated over a time interval starting at $t = 0$ and finishing at $t = t_{max}$ (t_{max} varied). Different t_{max} values are presented in Figure 3(b) by corresponding curves (in any real situation the integration time span is determined by the conditions of an experiment). Similar limb brightening of neutron emission is also obtained in focused beam models (G. Kocharov and Mandzhavidze, 1984, Hua and Lingenfelter, 1987a). Meanwhile the degree of anisotropy is somewhat less in the arch due to the fact that protons are focused while they move inside the real solar magnetic field (not *ad hoc*). The reason appears to be the directivity of neutron emission in the arch model lies in the anisotropy of the column density traversed by particles as they slow down (see Figure 8 in Paper I). We considered how alterations of S_p, h_μ/h_A, and R_A would affect the directivity of secondary radiation (Figures 4 and 5); t_{max} was chosen to be 200 s. It is clearly seen that the directivity of secondary emission is almost independent of the primary proton power law index S_p (Figure 4) and is too weak to depend on the arch length (Figure 5(b)). At the same time there is a significant dependence on the magnetic field scale in the chromosphere h_μ (Figure 5(a)). That should be linked to the fact that as the h_μ/h_A ratio increases, the anisotropy of column density traversed by particles in a given direction

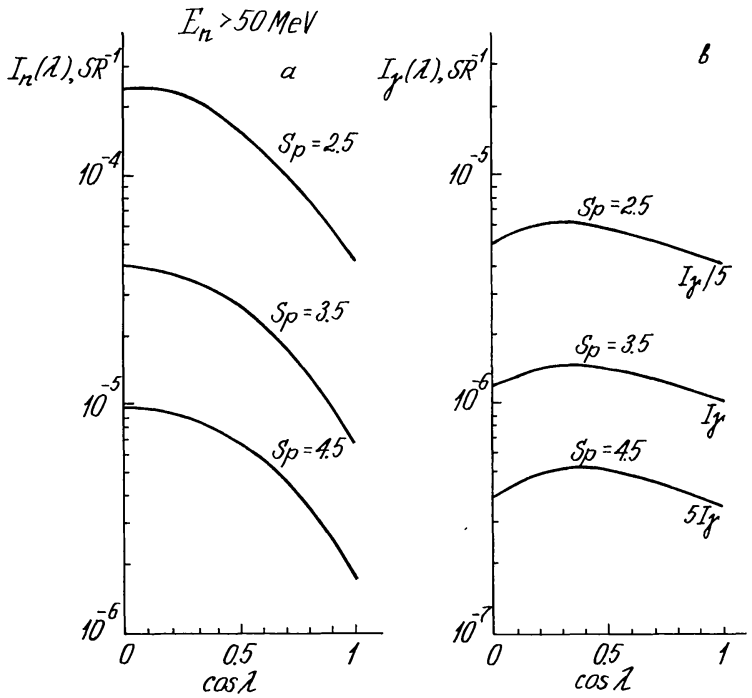

Fig. 4. Neutron (a) and π^0-decay γ-emission (b) versus angular distance from the flare site to the disk center, λ, for different power-law indices, S_p, of primary ion spectrum. $R_A = 10^9$ cm, $n_c = 10^{11}$ cm^{-3}, $n_0 = 10^{12}$ cm^{-3}, $h_\mu/h_A = 4$, the integration time $t_{max} = 200$ s, N_p (> 30 MeV) = 1.

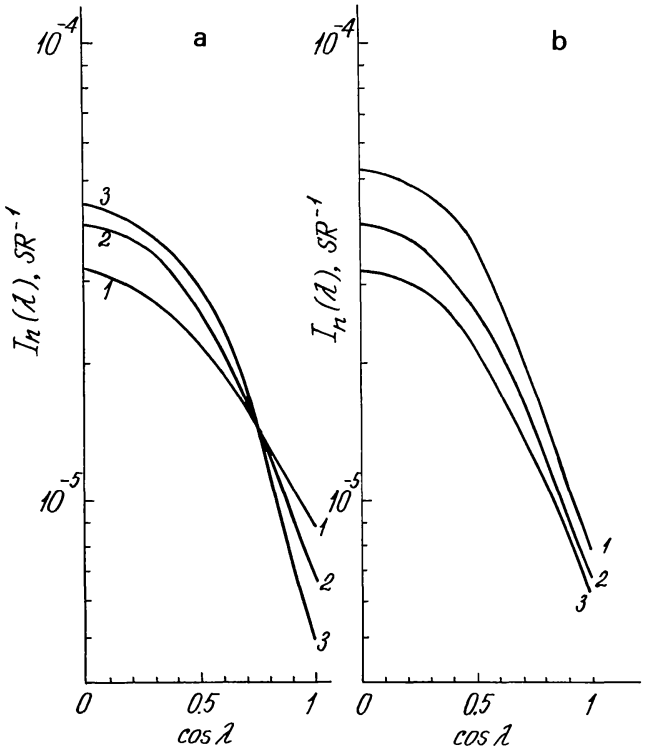

Fig. 5. Angular distribution of escaping neutrons (> 50 MeV) under different values of arch parameters. t_{max} = 200 s, N_p (> 30 MeV) = 1, S_p = 3.5, $n_c = 10^{11}$ cm^{-3}, $n_0 = 10^{12}$ cm^{-3}, $h_A = 2 \times 10^7$ cm. (a) $R_A = 10^9$ cm. (1) h_μ/h_A = 2. (2) h_μ/h_A = 4. (3) h_μ/h_A = 8. (*b*) h_μ/h_A = 4. (1) $R_A = 2 \times 10^8$ cm. (2) $R_A = 10^9$ cm. (3) $R_A = 5 \times 10^9$ cm.

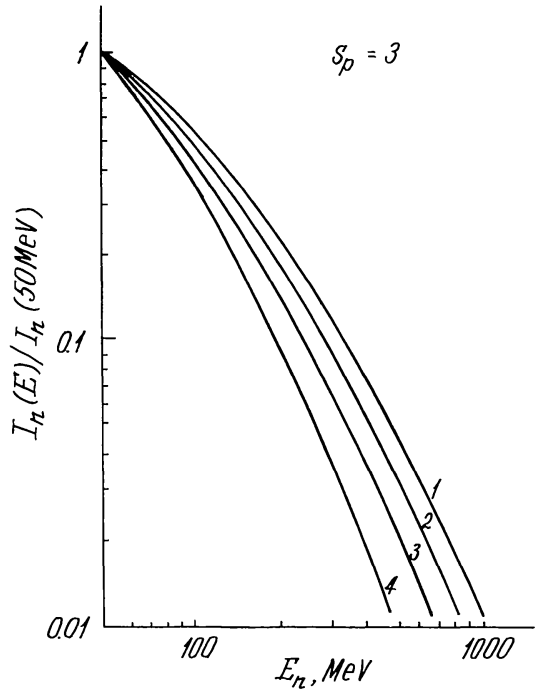

Fig. 6. Differential energy spectra of neutrons emitted in various longitude intervals (total over time). $R_A = 10^9$ cm, $n_c = 10^{11}$ cm^{-3}, $n_0 = 10^{12}$ cm^{-3}, $h_A = 2 \times 10^7$ cm, h_μ/h_A = 4. (1) $0 \le \cos\lambda \le 0.25$; (2) $0.25 \le \cos\lambda \le 0.5$; (3) $0.5 \le \cos\lambda \le 0.75$; (4) $0.75 \le \cos\lambda \le 1$.

also increases (see relations (13) and (14) in Paper I) and, correspondingly, secondary emission anisotropy increases.

The energy spectra of neutrons and γ-quanta are almost independent of the loop parameters and are determined mainly by the primary spectrum. Meanwhile there is a considerable dependence on the direction of emission. In Figure 6 we show neutron spectra averaged over different intervals of longitude. The spectrum hardens as the flare heliolongitude rises. The reason lies in the fact that the angular diagram of neutron production becomes narrower as the neutron energy increases. Note that the differential cross-section of neutron production is elongated along the velocity direction, as it is for the relativistic electron bremsstrahlung. As a result, neutron anisotropy is similar to that of bremsstrahlung γ-rays. One should keep in mind that the reasons why spectra become harder closer to the limb are different in those two cases.

SMM satellite experiment measured neutron fluxes ($E_n > 50$ MeV) at the Earth's orbit. Their time dependence is determined by the spectrum of neutrons ejected in a given direction. Therefore, while calculating neutron fluxes at the Earth's orbit we considered their dependence on primary ion spectrum as well as on flare longitude (Figure 7). It is clearly seen that as S_p increases the rise of $F_n(t)$ lasts longer because there are more neutrons of low energy. That effect does not depend on the propagation

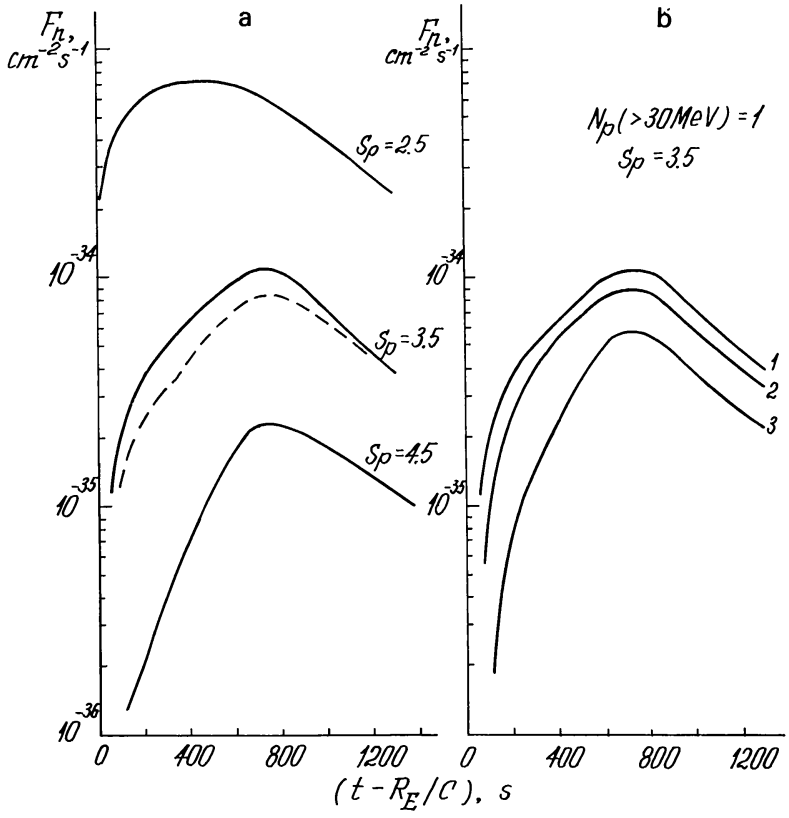

Fig. 7. (a) Neutron (> 50 MeV) time profiles at the Earth's orbit, R_E = 1 AU, for a limb flare ($\lambda = 90°$) under different values of the power-law index, S_p, of primary ions. N_p (> 30 MeV) = 1, $R_A = 10^9$ cm, $n_c = 10^{11}$ cm, $n_0 = 10^{12}$ cm^{-3}, $h_A = 2 \times 10^7$ cm. Solid lines: $h_\mu/h_A = 4$. Dashed line: $h_\mu/h_A = 8$. (b) Neutron (> 50 MeV) time profiles at the Earth's orbit for various flare sites. Arch parameters are the same as for the solid lines in Figure 7(a). (1) $\cos\lambda = 0$. (2) $\cos\lambda = 0.3$. (3) $\cos\lambda = 0.6$.

of primary particles in the solar atmosphere (see, e.g., Hua and Lingenfelter, 1987). As seen from Figure 7(b), limb flares yield a greater emission flux of a steeper rise in intensity.

As accelerated protons interact with the solar atmosphere they also produce π^0 which move preferentially along the direction of primary particle velocity and decay in flight. The number of π^0-decay γ-quanta following the velocity direction exceeds that in the reverse direction, and that is why the decay emission is anisotropic (Figure 4(b)). Nonetheless, the degree of directivity of π^0-decay γ-emission is significantly less than that of neutrons. Thus the model predicts the limb-brightening effect of high-energy neutrons. At the same time π^0-decay γ-emission anisotropy appears to be too small to provide for heliolongitude distribution of flares with detected fluxes of >10 MeV γ-radiation (Vestrand *et al.*, 1987). This indicates that the bulk of the radiation was produced by ultrarelativistic electrons (see Paper I).

3. Effect of Pitch-Angle Scattering on the Secondary Emission

Until now we have considered only the motion of accelerated particles in a regular magnetic field. We now assume that there is also a stochastic magnetic field B_{st} in the coronal part of the arch and $B_{st} \ll B_c$. That field causes the particles moving inside the arch to be scattered. Here we are going to consider the influence which the turbulence produced by exterior sources has upon the features of flare secondary emission.

The spectral energy density of the turbulent field is chosen to be $W(k) = W_0 k^{-\alpha}$, with the wave vector $k \geq k_0$, $k_0 = 1/L_0$, where L_0 stands for the main scale of turbulence. We assumed that $L_0 \gg R_L$, where R_L is the particle gyroradius. Carrying out the calculation one may use the value $\alpha = 1.5$ (see, e.g., Bykov and Toptyghin, 1981, and references therein). For that value of α the total turbulent energy density is

$$\frac{W}{B_c^2/8\pi} = 10^{-6}\left(\frac{v_0}{10^{-9}\ \mathrm{erg}^{1/4}\ \mathrm{cm}^{-5/4}}\right)\left(\frac{f_{\min}}{10\ \mathrm{Hz}}\right)^{-1/2}\left(\frac{n_c}{10^{10}\ \mathrm{cm}^{-3}}\right)^{-1/4}, \quad (1)$$

where $v_0 = \pi^2 B_c^{-3/2} W_0$ and $f_{\min} = v_A/L_0$, with v_A the Alfvén velocity. The stochastic component of the magnetic field brings about pitch-angle scattering of fast particles. Given that the magnetic field inhomogeneities are static, the equation for the distribution function of the fast particles takes the form (e.g., Toptyghin, 1983, Equation (9.28))

$$\frac{\partial f}{\partial t} + v\mu\,\frac{\partial f}{\partial \xi} = \frac{\partial}{\partial \mu}\left((1-\mu^2)\nu(\mu)\,\frac{\partial f}{\partial \mu}\right), \quad (2)$$

where $\mu = \cos\vartheta$, v and ϑ are particle velocity and pitch angle, and the ξ-axis is parallel to the regular magnetic field. Here we neglected the diffusion across the field. The second term in the left-hand side of Equation (2) describes the free movement of the particle at a velicity $v_\parallel = v\cos\vartheta$, and the right-hand side describes the pitch-angle diffusion. One should note that the angular dependence of the pitch-angle diffusion coefficient $\nu(\mu)$ is determined by the turbulence spectrum. In the case of one-dimensional turbulence

(given $\alpha = 1.5$) one obtains the following equation (which, e.g., can be derived from Equation (9.50) in Toptyghin, 1983):

$$\nu = \nu_0 \sqrt{\mu}\, v/\sqrt{p}\,, \tag{3}$$

where p is the rigidity of fast particles. The pitch-angle diffusion coefficient looks the same in the case of scattering on Alfvén waves with a one-dimensional spectrum given by $v \gg v_A$ (e.g., Ginzburg *et al.*, 1984, p. 258). Under the assumption of isotropic turbulence when μ is not very small, the ν coefficient has the same angular dependence but one more factor, which is ≈ 1 (Toptyghin, 1983, Equation (9.34)). Under the condition that $|\mu| \ll 1$ there is also a difference in the angular dependence $\nu(\mu)$ (Toptyghin, 1983; Fedorenko and Ostryakov, 1987).

As was shown in Paper I, when there is no turbulence the impulsive component of secondary radiation is produced by particles of small pitch angles ($\mu \geq \mu_c \approx 0.8$). These particles slow down quickly inside the dense regions at the base points of the magnetic arch. In the absence of turbulence there are no particles with $\mu \geq \mu_c$ after the end of the impulsive part of the burst. It is clear that weak pitch angle diffusion causes the particles to be 'pumped' over to the region $\mu \gtrsim \mu_c$. Due to Coulomb energy losses they slow down quickly in that range of μ and simultaneously produce secondary emission. Until the considered period is less than the characteristic scattering time of $\sim \pi/2$, the features of secondary emission do not depend on the behaviour of $\nu(\mu)$ in the region $|\mu| \ll 1$ because it is mostly the particles diffused under $\mu \lesssim \mu_c$ that are responsible for the emission. The form of the time-extended tails of the secondary emission will be influenced later by the dependence of $\nu(\mu)$ at small μ. But it seems to us that it is not timely to account for this effect. The way ν depends upon μ when μ is small is much more significant when, as the turbulence energy increases, the characteristic time of scattering becomes comparable with the arch flight time, $\pi R_A/v$.

The $\nu(\mu)$ dependence under small μ can significantly change the value of the spatial diffusion coefficient and, in particular, can make the diffusive regime of propagation impossible. So, provided μ is small one should take into account some additional processes, namely the resonance broadening effect and mirroring on long-wavelength fluctuations (Achterberg, 1981, Holman, Ionsson, and Scott, 1979; Toptyghin, 1983). Now we are going to estimate the influence of Cherenkov resonance broadening following Toptyghin (1983). According to his estimation (9.74), and provided the turbulence is isotropic, the transport mean free path along the magnetic field is

$$\Lambda \approx \frac{B_c^2}{\langle B_{st}^2 \rangle} \left(\frac{L_0}{R_L}\right)^{\alpha - 1} \frac{R_L}{x_0^{\alpha - 1}}\,, \tag{4}$$

where x_0 is the absolute value of that pitch-angle cosine under which the $\nu(\mu)$ coefficient is minimal. Relations similar to (3), which is obtained in the linear theory, are valid only when $|\mu| > x_0$. As a result of Cherenkov resonance broadening, x_0 increases with $\langle B_{st}^2 \rangle$.

The mean free path becomes the important parameter of the problem if it is small

enough. Consider the turbulence level which equalizes the arch flight time and the time of scattering. Equalizing Λ and the arch length πR_A and using the relations between x_0 and the turbulence energy level (Equations (9.40) and (9.46) from Toptyghin, 1983) one can obtain:

$$x_0 = \left(\frac{v_A}{\pi R_A f_{\min}}\right)^{1/3(\alpha+1)} \left(\frac{v}{v_A}\frac{f_{\min}}{\omega_i}\right)^{(3-\alpha)/6(\alpha+1)}, \tag{5}$$

where ω_i is the proton Larmor frequency. One can see that $x_0 = 0.23$ for $R_A = 10^9$ cm, $n = 10^{11}$ cm^{-3}, $B_c = 100$ G, $v = 10^{10}$ cm s^{-1}, $\alpha = 1.5$, and x_0 is not very sensitive as regards the alterations of parameters. Hence, the form-factor $x_0^{\alpha-1}$ in (4) is not very small ($x_0^{1/2} \approx 0.5$). As the turbulence energy increases, Λ becomes less than πR_A and the form-factor $x_0^{\alpha-1}$ is shifted towards 1. So taking the ν angular dependence into account does not change the order of magnitude of the transport mean free path. We note that under the accepted parameter values and $T \leq 10^7$ K, the ratio of the gasokinetic pressure to the magnetic pressure ($\beta \ll 1$) is what makes the influence of the turbulence spectrum limits upon Λ (considered by Holman, Ionsson, and Scott, 1979 and Achterberg, 1981) insignificant. It follows from the discussion that it is reasonable to omit the angular dependence of pitch angle diffusion coefficient as first approximation. For example, one may suggest:

$$\nu = \nu_0 v/\sqrt{p}\,. \tag{6}$$

Such a choice makes it possible to simplify the solution of the problem without qualitative errors. The quantitative alterations meanwhile do not exceed theoretical and experimental uncertainties. Relation (6) corresponds to the following for the transport mean free path of 100 MeV protons:

$$\frac{\Lambda_1}{\pi R_A} \approx 2 \times 10^2 \left(\frac{10^{-9}\ \text{erg}^{1/4}\ \text{cm}^{-5/4}}{\nu_0}\right)\left(\frac{10^9\ \text{cm}}{R_A}\right). \tag{7}$$

Provided the stochastic component of the magnetic field is determined by MHD-waves of small amplitude, one should insert into Equation (2) certain terms describing acceleration (see, e.g., Ginzburg *et al.*, 1984, p. 257). The acceleration process is $(v/v_A)^2$ times slower than the scattering process. The characteristic acceleration time is $\tau_A \approx (v/v_A)^2 \nu^{-1} \gg \nu^{-1}$. As seen from the qualitative consideration given above, which is also supported by the calculation results to be presented below, the time of particle propagation inside the arch is $\lesssim \nu^{-1}$ provided the turbulence level is not very high. One may neglect acceleration over such a time. We limit our consideration to parameter values under which the main part of the secondary emission impulse is generated during a time much less than τ_A. In this case one may omit the acceleration terms of the kinetic equation. So the problem one now faces is to consider the processes described by Equation (2) with the ν coefficient extracted from (6). We also took into account the Coulomb losses. The Monte Carlo calculations were used to consider the propagation of accelerated particles and the production of secondary emission (see Appendix II).

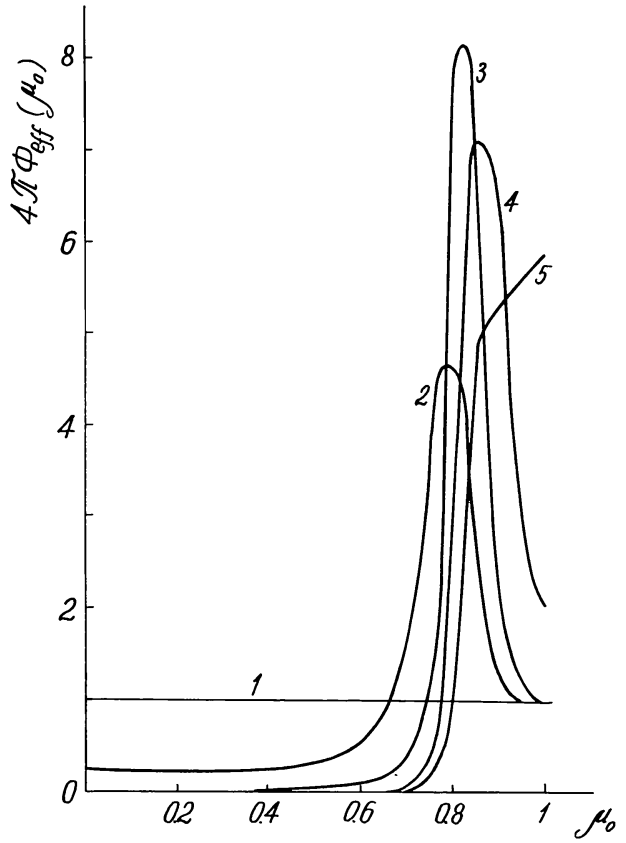

Fig. 8. Effective angular distribution of ions at the top of the arch for different levels of turbulence. $R_A = 10^9$ cm; $n_c = 10^{11}$ cm^{-3}; $n_0 = 10^{12}$ cm^{-3}; $h_A = 2 \times 10^7$ cm; $h_\mu/h_A = 4$; $4\pi \int \phi_{eff}(\mu)\, d\mu = 1$. (1) No pitch-angle diffusion ($\nu_0 = 0$). (2–4) Weak pitch-angle diffusion: (2) $\nu_0 = 10^{-10}$ erg$^{1/4}$ cm$^{-5/4}$. (3) $\nu_0 = 10^{-9}$ erg$^{1/4}$ cm$^{-5/4}$. (4) $\nu_0 = 10^{-8}$ erg$^{1/4}$ cm$^{-5/4}$. (5) Moderate pitch-angle diffusion, $\nu_0 = 4 \times 10^{-7}$ erg$^{1/4}$ cm$^{-5/4}$.

The results of calculations are presented in Figures 8 to 11 for different levels of turbulence energy. Considering > 50 MeV neutron generation by accelerated protons we plotted the distribution of protons which had produced secondary emission against the pitch-angle recalculated to the top point of the arch (as though the transverse adiabatic invariant were conserved): $\phi_{eff}(\mu_0)$, where $\mu_0 = \sqrt{1 - (1 - \mu_{int}^2)B_c/B(\xi_{int})}$ is the recalculated pitch-angle cosine, μ_{int} and ξ_{int} stand for the proton pitch-angle cosine and its coordinate at the moment of interaction respectively, and B_c is the magnetic field value at the arch top. Over all, the time interactions were taken into account. Such a procedure yields the effective angular distribution at the arch top, i.e., the kind of proton distribution which, in the case of no turbulence, would provide the same secondary emission directivity as that coming as a result of scattering on turbulence. In Figure 8 $\phi_{eff}(\mu_0)$ is depicted under the assumption that the initial angular distribution of accelerated protons was isotropic. It is clear that weak pitch-angle diffusion (curves 1–4) is effective to pump up the number of particles to pitch angles close to the loss cone boundary, μ_l. The scattering frequency ν is too small to fill the loss cone. In this case the maximum value of $\phi_{eff}(\mu_0)$ is determined by the balance of the angular velocity and of the deceleration velocity $1/T_d$ (for T_d see Figure 7 in Paper I). Hence,

the maximum undergoes translocation towards lesser pitch angles (higher $1/T_d$) as the turbulence energy increases. When the turbulence energy is as high as to make $\Lambda < \pi R_A/(1 - \mu_l)$ valid, the process of filling up the loss cone gets under way (curve 5 in Figure 8). It is what is called the moderate pitch-angle diffusion regime (see, e.g., Bespalov and Trahtengertz, 1980). Although the pitch-angle diffusion is sufficient to fill up the loss cone in the regime, the spatial diffusion coefficient $D = \frac{1}{3}\Lambda v$ is still large enough to keep the number density of accelerated protons constant all along the arch length. Assuming also that there is no scattering inside the magnetic mirror regions in the chromosphere, one can obtain the flux of precipitating protons:

$$\frac{dN}{dt} = \frac{N}{2\pi R_A} v(1 - \mu_l^2), \tag{8}$$

i.e., the total number of particles inside the loop as well as the rate of precipitation and, consequently, the emission rate will decay exponentially with the characteristic time

$$\tau_M = \frac{2\pi R_A}{v(1 - \mu_l^2)} . \tag{9}$$

The regime of moderate diffusion suggests that (9) is larger than the diffusion time $\tau_D = (\pi R_A)^2/4D$ which yields $\Lambda \gtrsim (1 - \mu_l^2)R_A$. For those propagation modes the results

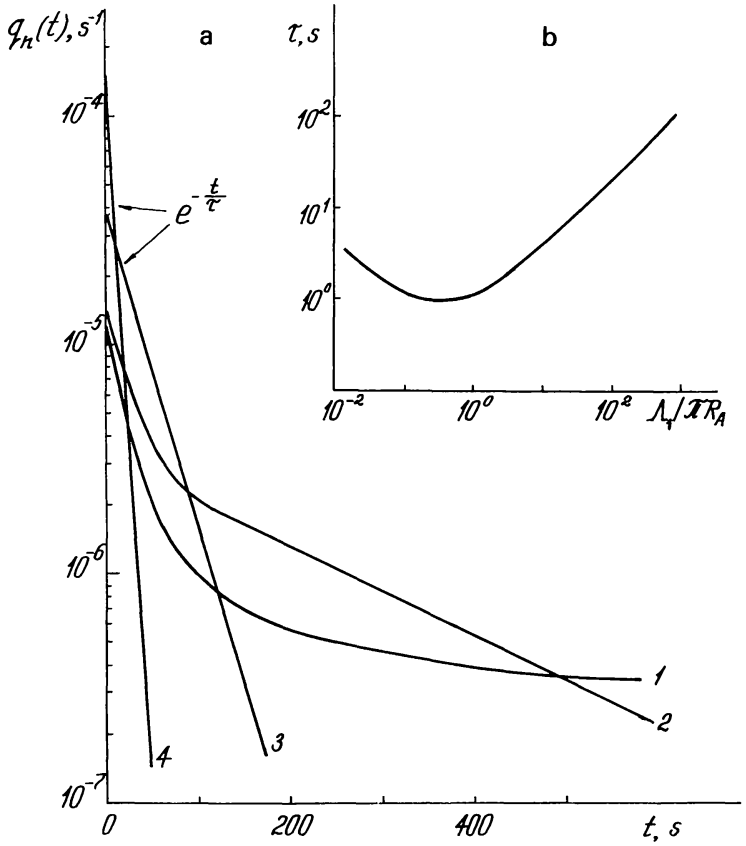

Fig. 9. (a) Neutron (> 50 MeV) generation rate versus time. $S_p = 3.5$, N_p (> 30 MeV) = 1. Parameters of the arch and curve numeration are the same as in Figure 8. (b) Neutron generation rate decay time versus transport mean free path Λ_1.

of Monte Carlo simulations are shown in Figure 9(a). It is clear that as the turbulence energy increases in the weak pitch-angle diffusion regime a power-law decay in the rate of the secondary emission generation transforms into an exponential one. The decay characteristic time decreases and finds its minimum value in the moderate pitch-angle diffusion mode. That value is in accordance with estimation (9). If the turbulence energy density continues to increase, the system passes over into the intense pitch-angle diffusion regime ($\Lambda \ll (1 - \mu_l^2)R_A$) where the spatial diffusion time τ_D becomes larger than the time of precipitation into the loss cone (9). As the turbulence energy increases, the diffusion coefficient D decreases and it takes increasingly more time for a particle to escape from the arch (Figure 9(b)).

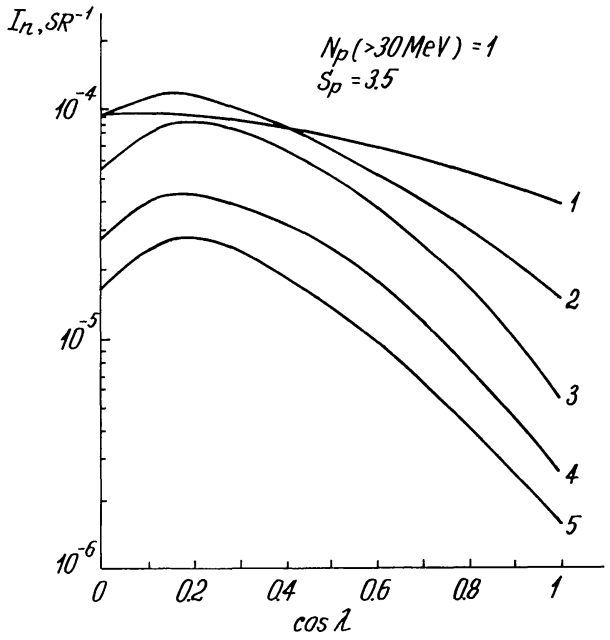

Fig. 10. Angular distribution of escaping neutrons (> 50 MeV). Total over time. λ is the angular distance from the flare site to the disk center. Parameters of the arch and curve numeration are the same as in Figure 8.

Figure 10 makes it clear that in the weak pitch-angle diffusion regime (curves 2, 3, 4) the flux anisotropy of escaping neutrons increases as Λ decreases. Meanwhile, the total number of escaping neutrons becomes significantly smaller. The reason is that most of the neutrons are generated by protons moving downwards. In this case the limb absorbtion is considerable because neutrons are likely to be generated more deeply. As the turbulence energy increases, the distribution function inside the arch becomes almost isotropic, hence, the angular distribution of secondaries becomes particularly independent on the turbulence energy density (this distribution is presented by curve 5). It is seen in Figure 11 that the maximal neutron flux value at the Earth's orbit alters only slightly compared to the number of escaping neutrons (Figure 10) because the effect of the decreasing number of escaping neutrons (as v_0 increases) and that of the decreasing generation time-scale tend to compensate each other.

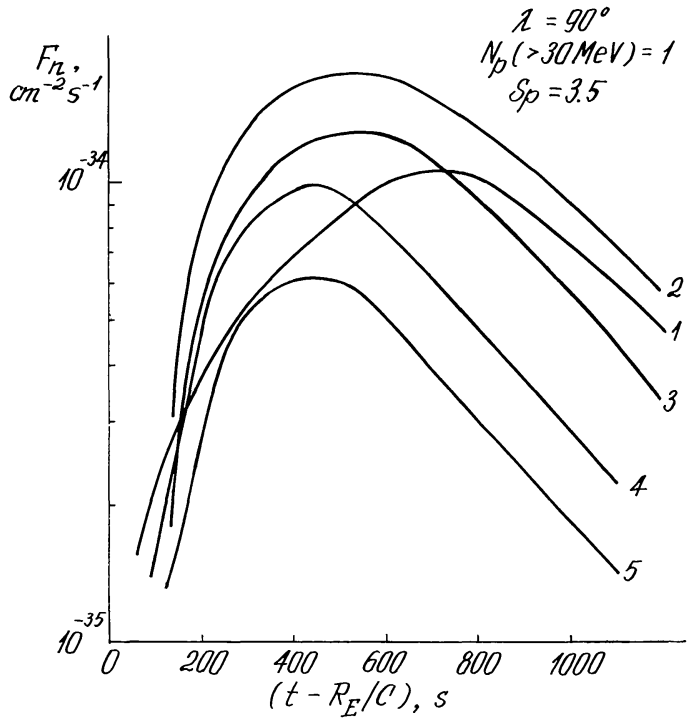

Fig. 11. Neutron (> 50 MeV) time profiles at the Earth's orbit, R_E = 1 AU, for a limb flare. Parameters of the arch and curve numeration are the same as in Figure 8.

As a conclusion we would like to note that in the intense pitch-angle diffusion regime the main part of the secondary radiation is produced during a time $t \sim \tau_D$. As far as we neglect the acceleration which accompanies scattering on MHD-waves we have to keep in mind that our consideration suggests the diffusion time τ_D to be much less than the acceleration time, τ_A. This restriction yields $\Lambda/\pi R_A \gg v_A/v \sim 10^{-2}$, i.e., $W \ll 10^{-2} B_c^2/8\pi$ at $f_{\min} = 10$ Hz, $n_c = 10^{11}$ cm^{-3}, and $R_A = 10^9$ cm.

4. Effect of Cyclotron Instability on the Dynamics of Secondary Particle Production

G. Kocharov, L. Kocharov, and Kovaltsov (1981) highlighted that trapping of accelerated particles within a dispersed region would make it possible to account for the late impulsive maximum in γ-ray lines as compared to X-radiation maximum (without the assumption of a second acceleration phase during a flare). The trapping can come as a result of the formation of toroidal closed magnetic configurations due to magnetic field line reconnection or, as suggested by Bespalov, Zaitsev, and Stepanov (1986), of 'turbulent mirrors' due to the instability of the proton distribution function and generation of Alfvén waves. Inasmuch as we considered the loop structure above, let us now consider in more detail the generation of Alfvén waves by cyclotron instability.

The source of the instability is the anisotropy of the distribution function of accelerated protons. The anisotropy arises from the removal of small pitch-angle particles. The accelerated particles of velocity v and number density n_p amplify resonant waves of

frequency $\omega = (v_A/v)\omega_i$; where ω_i is the proton Larmor frequency. The amplification increment $\gamma \approx n_p\omega_i^2/(n\rho\omega)$, where n is the background plasma density and $\rho = B_{ph}/B_c$ is the mirror ratio. It is just these waves on which the protons scatter (Zaitsev and Stepanov, 1985). It is known (see, e.g., Alexandrov, Bogdankevich, and Rukhadze, 1978) that Alfvén waves dissipate due to collisions. The decrement is $\delta = (m_e/m_p)\nu_e$, where ν_e is the electron collision frequency. In order to develop the instability it is necessary to have $\gamma > \delta$. Therefore, instability develops neither in a large arch (small n_p) nor in a dense and cold plasma (great ν_e). Now we consider the case when the instability increment is rather high and the Alfvén waves are amplified due to cyclotron instability. Bespalov and Trahtengertz (1980) and Bespalov, Zaitsev, and Stepanov (1986) show that in this case an intense pitch-angle diffusion regime can develop and the flux of protons $q = \zeta n_p v_A$, where the dimensionless factor ζ does not differ much from 1.

As a result of penetration of accelerated protons through the turbulent layers at the trap ends (after the acceleration is over), the number N of protons inside the arch decreases:

$$\frac{dN}{dt} = -\frac{N}{\tau_s}, \tag{10}$$

where $\tau_s = \pi R_A/(2\zeta v_A)$. Now it becomes clear that the particle escape rate dN/dt, as well as the generation rate of secondary products, decay in this regime exponentially:

$$I(t) \sim e^{-t/\tau_s}. \tag{11}$$

Note that in the considered regime of intense self-consistent pitch-angular diffusion, τ_s does not depend upon the number of accelerated particles. The reason is that the turbulence is automatically fixed at the level where the flux velocity of accelerated protons coincides with the Alfvén velocity.

5. Solar Flares with High-Energy Neutron and π^0-Decay Gamma-Ray Emission

In this section we apply our treatment to the flares of 3 June, 1982, 21 June, 1980, and 7 December, 1982 for which high-energy neutrons and γ-rays above 10 MeV were detected by the Gamma-Ray Spectrometer (GRS) on board the SMM satellite (Chupp *et al.*, 1982; 1985, 1987; Forrest *et al.*, 1985; Rieger *et al.*, 1987).

One of the uncertainties in deriving time-dependent fluxes and energy spectra of neutrons from GRS measurements is related to the inability of GRS to measure neutron energy. Therefore, they are deduced by the time-of-flight method assuming a certain time dependence of neutron production at the Sun. It is commonly accepted that neutrons are produced simultaneously with the 4–7 MeV nuclear de-excitation lines. This leads to the conclusion that the observations of 3 June, 1982 and 21 June, 1980 are inconsistent with the assumption of power-law primary energy spectra (Hua and Lingenfelter, 1987a; Murphy and Ramaty, 1984; Murphy, Dermer, and Ramaty, 1987). In fact it is supposed that both low (tenth of MeV) and high (hundreds of MeV) energy particles

responsible for production of γ-ray lines and high-energy neutrons or pions (respectively) interact immediately. However, the lifetimes of particles of these two groups in magnetic loops may differ by orders of magnitude resulting in different time profiles of high- and low-energy emission (the situation actually observed during the 3 June, 1982 flare).

To avoid the uncertainties in our analysis we attempt to fit directly the GRS counting rates above 10 MeV using the sensitivities presented by Chupp *et al.* (1987) and Cooper *et al.* (1985). In our Monte Carlo simulations in all cases the loop parameters were taken to be: $n_c = 10^{11}$ cm^{-3}; $n_0/n_c = 10$; $h_\mu/h_A = 6.7$; $h_A = 2 \times 10^7$ cm; $R_A = 10^9$ cm. However, there remains a certain freedom of choice because in the presence of plasma turbulence pitch-angle scattering becomes the dominant process determining the radiation production rates and masks the dependence of fluxes upon the loop parameters.

(1) 3 June, 1982 (S 09 E 72, 11:41 UT). This flare has been extensively treated by several authors (Murphy and Ramaty, 1984; G. Kocharov, Mandzhavidze, and Gueglenko, 1987; G. Kocharov *et al.*, 1987; Kovaltsov and L. Kocharov, 1987a, b; Ramaty and Murphy, 1987; Hua and Lingenfelter, 1987a, b; Murphy, Dermer, and Ramaty, 1987). The particular feature of the observations was the difference in the time profiles of emission in the different energy bands. Duration of the 4–7 MeV γ-ray line emission as well as hard X- and power-law continuum γ-radiation was approximately 60 s while high-energy neutrons and pions were produced for about 20 min after the first impulsive phase of the flare (Chupp *et al.*, 1985, 1987; Forrest *et al.*, 1985). Murphy, Dermer, and Ramaty (1987) proposed the existence of a second phase acceleration process which lasted about 20 min and generated particles with an extremely hard spectrum responsible for the production of pions at the extended phase of the flare.

On the other hand, the situation of the kind observed on 3 June, 1982 occurs naturally in our model. Indeed, as was shown in the Paper I time-scales of 4.4 MeV line and high-energy electron bremsstrahlung radiation production are of the order of seconds but hundreds of seconds for the high-energy neutrons and pions.

We propose that particles are accelerated in a single acceleration process lasting about 1 min and the acceleration rate follows the 60 s peak of the 4–7 MeV radiation. To explain the observed second maximum of the π^0-decay γ-radiation intensity (Chupp *et al.*, 1987; Forrest *et al.*, 1986) we suggest a fast rise of MHD turbulence in the coronal part of the loop causing the increase of pitch-angle scattering rate and precipitation of the trapped particles. Such a rise of turbulence might be caused by shock wave propagation through the corona. Note that the start of a type II radio burst, which is commonly attributed to the coronal shocks, was reported at 11:44 UT (*Solar Geophys. Data*, 1982). The calculated production rate of π^0-decay γ-rays is shown in Figure 12. The pitch-angle scattering was 'switched on' at the end of the impulsive phase with the initial value of $\nu_0 = 1.3 \times 10^{-10}$ erg$^{1/4}$ cm$^{-5/4}$ which linearly decreased to the value $\nu_0 = 5 \times 10^{-12}$ by the end of the flare ($\approx$11:59 UT).

Another cause of the secondary γ-emission maximum may well be the 'atmospheric evaporation' which brings about an increase in matter density at the generation site. Kovaltsov and L. Kocharov (1987) show that if matter density increases 50-fold by the 120th second after the impulsive phase start, it is possible to fit the π^0-decay γ-radiation time profile observed on 3 June, 1982.

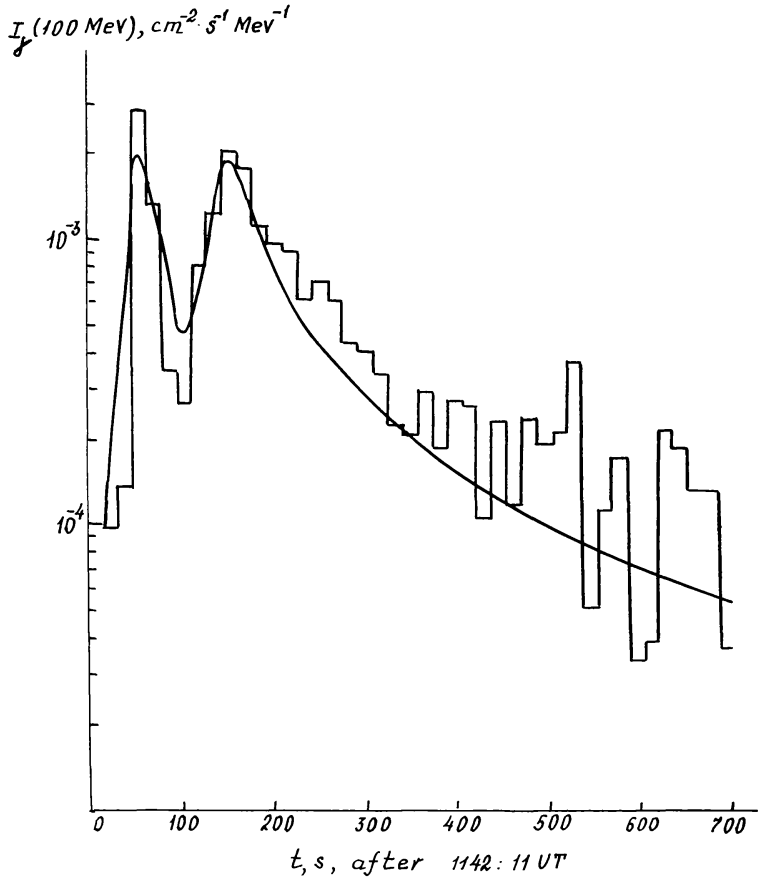

Fig. 12. 3 June, 1982. Time-dependent intensity of γ-emission (Chupp *et al.*, 1987). The curve is the time profile obtained by means of the Monte Carlo simulation technique. $n_c = 10^{11}$ cm^{-3}, $n_0 = 10^{12}$ cm^{-3}, $h_\mu/h_A = 6.7$, $R_A = 10^9$ cm, v_0 – see text.

120th second after the impulsive phase start, it is possible to fit the π^0-decay γ-radiation time profile observed on 3 June, 1982.

So the γ-radiation peculiarities of the event may be explained without the assumption of the second (prolonged) acceleration phase. The lot of particles are accelerated during the impulsive phase and the second π^0-decay γ-radiation peak comes as a result of some unstationary processes developing in the arch after the impulsive phase.

It is interesting to note that the ratio of π^0-decay γ-radiation emitted during the impulsive phase to the total ($\approx 20\%$) is in agreement with the assumption of an isotropic initial distribution of accelerated ions at the top of the loop (see Section 3 of Paper I). In this case, the calculated intensity decay rate is also close to that observed.

To account for the observed π^0-decay γ-emission intensity on 3 June, 1982 it is necessary to have as many as $N \approx 10^{31}$ initial protons of $E > 300$ MeV. Assuming the volume of the arch (or arches) to be 2×10^{27} cm^3 we obtain the initial density of accelerated particles as $n_p = 5 \times 10^3$ cm^{-3}. Let us estimate the cyclotron instability increment for the waves resonant to these protons: $\gamma \approx 0.7 \sqrt{n/10^{12}\ \text{cm}^{-3}}\ \text{s}^{-1}$ (when the mirror ratio $\rho \approx 4$). Under the accepted parameter values the wave dissipation decrement $\delta \geq \gamma$ under $T \leq 1.4 \times 10^6 (n/10^{11}\ \text{cm}^{-3})$ K. Hence, $\delta > \gamma$ later when N is less than its initial value. In this case dissipation through collisions suppresses the

instability and the resonant Alfvén waves are not amplified. That is why we were right to neglect the scattering of protons responsible for π^0-decay γ-radiation on self-derived turbulence even for the 3 June, 1982 event, which was powerful in γ-rays.

On the other hand, the number of $E > 10$ MeV protons responsible for γ-ray line generation is approximately 3 orders of magnitude greater. Correspondingly, the amplification increment for resonant waves is higher. Therefore, one cannot neglect the scattering caused by the turbulence. As one can see in Figure 13, there is an almost

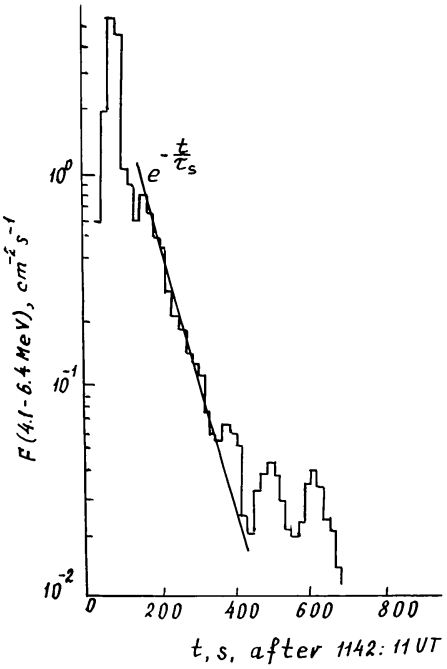

Fig. 13. 4.1–6.4 MeV γ-emission for 3 June, 1982 event. The experimental curve is from Ramaty and Murphy (1987), the theoretical line is from Kocharov *et al.* (1988).

exponential decay with a characteristic time ≈ 80 s in the time profile of the 4–7 MeV emission. This feature can be explained in terms of proton escape in the regime of intense pitch-angle diffusion on self-consistent turbulence (Section 4). In this case the arch parameters obey the relation $R_A = 3.5 \times 10^9 \zeta (B_c/100\ \mathrm{G})\,(10^{11}\ \mathrm{cm}^{-3}/n_c)^{1/2}$ cm. Hence, the observations of γ-emission find an explanation if one assumes that protons accelerated during the impulsive phase are kept within a loop of $\approx 10^{10}$ cm length. Note that the π^0-decay γ-radiation decay time depends only slightly upon the loop length (Kovaltsov and L. Kocharov, 1987a, b) which is, therefore, determined only in γ-ray line decay time observations. Hence, we conclude that on 3 July, 1982 the accelerated protons were kept inside a rather large loop. On the other hand, the characteristic time of the impulsive flares is about several seconds. The corresponding arch length is about 10^9 cm. It is reasonable to assume that on 3 June, 1982 protons that initially accelerated inside a small arch were later trapped in a larger one of $\approx 10^{10}$ cm length. In this model one can explain the delayed switch-on of exterior turbulence in the large arch in terms

of the time it took the perturbation to propagate from a compact energy source at $\approx 10^8$ cm s^{-1} velocity.

In our calculations, the primary energy spectrum of accelerated particles was supposed to be a power law in energy per nucleon. The best fit of the calculated neutron spectrum emitted at a direction 72° to the measured one leads to $S_p = 3.4$ (Figure 14).

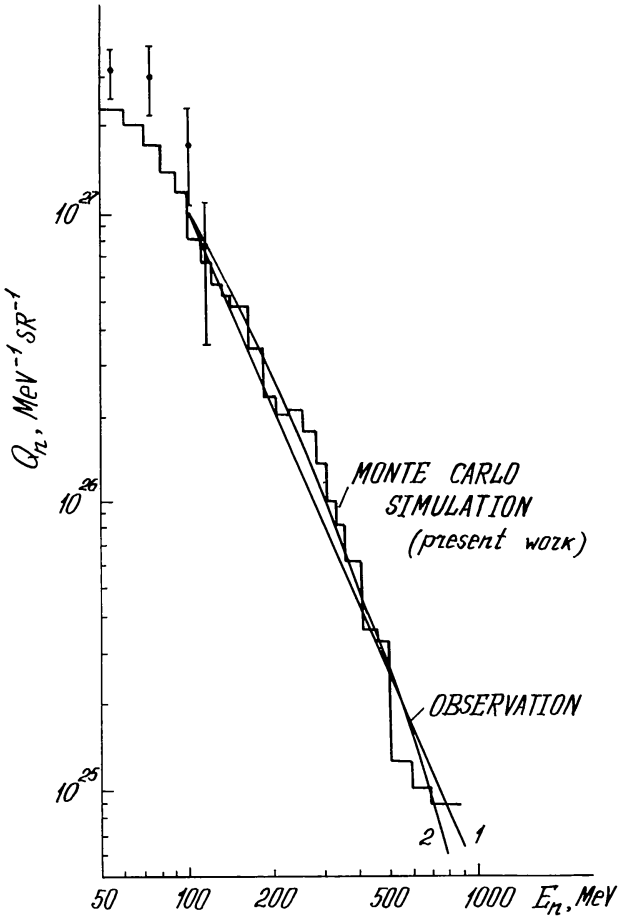

Fig. 14. 3 June, 1982. Energy spectrum of neutrons emitted in the direction of Earth ($\lambda = 72°$). The curves are the best fits to the data (power-law (1) and Bessel function (2) with parameters $S_n = 2.4$ and $\phi = 0.07$ (Chupp *et al.*, 1987)). The dots are from Evenson *et al.* (1985).

The number of accelerated particles N_p (> 30 MeV) = 2×10^{33} was then derived by comparing the total number of detected neutrons above 100 MeV of 8×10^{28} sr^{-1} (Chupp *et al.*, 1987) with the calculated value at the 72° emission angle. In Figure 15 we also present the measured and calculated GRS counting rates of > 50 MeV neutrons.

Next we calculated intensities of the other components of γ-radiation produced by these particles: π^0-decay γ-rays, 4–7 MeV nuclear de-excitation lines, 2.2 MeV ($np \rightarrow d\gamma$) line and 0.511 MeV positron annihilation line. To calculate 2.2 MeV and 0.511 MeV line intensities we used the results of Murphy and Ramaty (1984) and Hua and Lingenfelter (1987b). We account for the Fe enrichment observed in the event (McDonald and Van Hollebeke, 1985) which causes an increase of 2.2 MeV flux

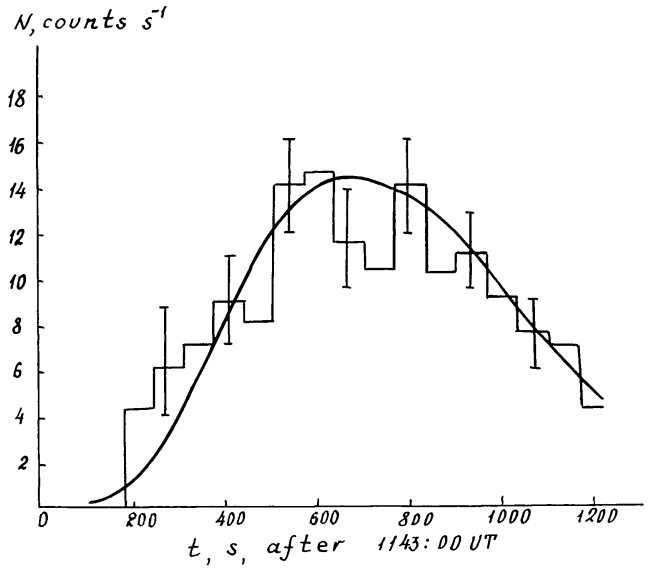

Fig. 15. 3 June, 1982. Measured by Chupp *et al.* (1987) and calculated SMM GRS counting rates of > 50 MeV neutrons.

(Abramov and Kotov, 1987). In all cases, the calculated values turned out to be very close to those measured (Table I).

(2) 21 June, 1980 (N20 W89, 01:18 UT). This was the first flare for which SMM GRS detected solar neutrons (Chupp *et al.*, 1982). The GRS counting rate above 10 MeV during this event is shown in Figure 16. We also present calculated counting rates of > 50 MeV neutrons and π^0-decay γ-radiation provided particle acceleration rate follows the 4–7 MeV radiation intensity (Chupp *et al.*, 1982). The primary spectra power-law index was chosen to obtain correct values of the ratios of neutrons to π^0 and neutrons to 4–7 MeV flux ratios. That leads to $S_p = 3.8$. The absolute normalization of N_p (> 30 MeV) = $(5 \pm 1) \times 10^{32}$ has been obtained from the best fit of the calculated neutron counting rate to the data.

TABLE I

Gamma-ray fluences

	3 June, 1982		21 June, 1980	
	Calculated	Measured	Calculated	Measured
F_γ (4–7 MeV) cm^{-2}	312 ± 31	305 ± 30 [1][b]	88 ± 18	76 ± 1.2 [1][b]
F_γ (0.511) cm^{-2}	140 ± 14	103 ± 8 [2][b]	29.8 ± 6.0	20.1 ± 4.6 [2, 3][b]
F_γ (2.2) cm^{-2}	290 ± 29	314 [4][b]	3.1 ± 0.6	3.1 ± 0.2 [5][b]
	π^0-decay γ-rays, F_γ (> 10 MeV)			
Impulsive phase (up to 60 s)	12.9 ± 1.3	12 [6][b]	1 ± 0.2	0.6 [7][b]
Total for the whole flare	53 ± 5	55 [6][b]	0.9 ± 0.2[a]	0.5 ± 0.2[a] [7][b]

[a] After 01:24:00 UT.

[b] (1) Rieger *et al.* (1983). (2) Share *et al.* (1983). (3) Hua and Lingenfelter (1987a). (4) Prince *et al.* (1983). (5) Chupp *et al.* (1982). (6) Forrest *et al.* (1986). (7) Forrest *et al.* (1985).

It can be seen that in the first minute the radiation mainly consists of high-energy electron bremsstrahlung with a small portion of π^0-decay γ-rays. However, in the extended phase (after 01:24 UT) the counts were completely due to neutrons. This is consistent with the analysis carried out by Chupp *et al.* (1985) and Forrest *et al.* (1985). The calculated fluence of π^0-decay γ-radiation in the first minute is about 1 cm^{-2} and 0.9 cm^{-2} in the extended period. While close to the measured values (see Table I), this is still a bit higher. However, it was admitted by Forrest *et al.* (1985) that π^0-decay γ-ray flux might be somewhat higher, provided there is a steepening of the power law continuum around 40 MeV.

In Table I we also present the calculated fluences of 4–7 MeV, 2.2 MeV, and 0.511 MeV γ-ray lines. The large uncertainties are due to the large errors in the GRS counting rates above 10 MeV (see Figure 16) resulting in uncertainty in the total number of accelerated particles. However, as for 3 June, 1982 the calculated values are quite close to those measured.

It follows from our calculations that the number of > 50 MeV neutrons emitted in the $\lambda = 89°$ direction was 2.8×10^{28} sr^{-1} with $E^{-2.9}$ energy spectra. After the first minute the neutron production rate decayed exponentially with a time constant of 200 s.

(3) 7 December, 1982 (S 19 W 86, 23:41 UT). The time profiles of neutral radiation detected during this flare were presented by Rieger *et al.* (1987) and are shown in

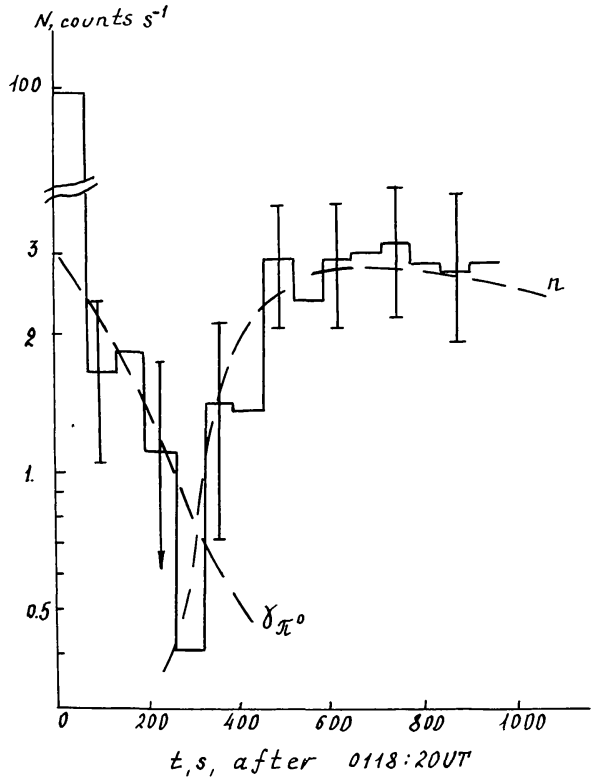

Fig. 16. 21 June, 1980. Measured by Chupp *et al.* (1985) and calculated counting rates of SMM GRS above 10 MeV. $v_0 = 10^{-10}$ $erg^{1/4}$ $cm^{-5/4}$.

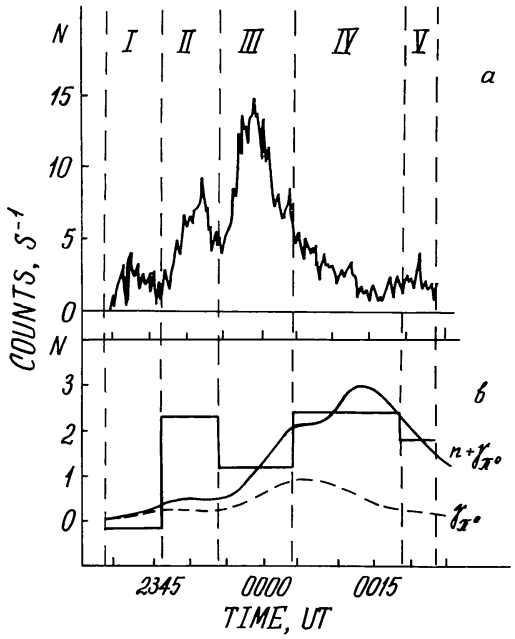

Fig. 17. Time history of the 7 December, 1982 flare. (a) 4–7 MeV band (Rieger *et al.*, 1987). (b) > 10 MeV band. Curves – calculations; histogram – measurements. $v_0 = 0$.

Figure 17. Again, as in the case of 3 June, 1982, GRS counting rates above 10 MeV do not follow the time history in the 4–7 MeV energy band. Ramaty and Murphy (1987) consider the > 10 MeV counting rate increase towards the end of the flare as an indication of second phase acceleration.

On the contrary we propose that the excess counts are due to the arrival of high-energy neutrons generated by the same particles which produced the 4–7 MeV γ-ray lines. To confirm this we modelled the acceleration rate after the 4–7 MeV intensity and calculated GRS counting rates of > 50 MeV neutrons and π^0-decay γ-radiation. The results are presented in Figure 17(b). The primary energy spectrum was taken as a power law with $S_p = 3.7$ and normalized to the 4–7 MeV γ-ray line fluence of 156 cm^{-2} (Rieger *et al.*, 1987) which leads to N_p (> 30 MeV) = 8.5×10^{32}.

Using the data of Rieger *et al.* (1987) we divided the whole observation period into five sections corresponding to the major peaks in the 4–7 MeV intensity, and for each time interval obtained measured GRS mean counting rates which are shown by the horizontal lines of the histogram. It can be seen that, except for the second interval, the measurements are well fitted by the calculated curve, and the intensity rise at the end of the flare (Sections IV and V) is mainly caused by neutrons. The excess counts in the second period are probably attributed to high-energy electron bremsstrahlung emission.

Thus we have analysed three different flares and it can be concluded that in each case the available data on γ-ray and neutron emission can be fully explained by the common model assuming that radiation was produced by the particles accelerated in a single acceleration process and then trapped in the magnetic loop. The single power-law spectra with similar indices provide good fit to the data.

Of course this does not exclude the possibility of the second phase acceleration

occurring somewhere higher in the corona and being responsible for the production of particles detected in interplanetary space, because in all flares considered, the energy spectra of detected particles were harder than those producing radiation (Rieger *et al.*, 1987; McDonald and Van Hollebeke, 1985). Another reason that might cause the difference lies in the energy dependence of particle escape rates from magnetic loops.

6. Conclusion

Murphy and Ramaty (1984), Hua and Lingenfelter (1987a), and Murphy, Dermer, and Ramaty (1987) considered the way accelerated particles interact with the solar atmosphere medium, neglecting the magnetic field influence on their motion. That leads to an almost instantaneous generation of secondary emission. Accordingly, an explanation of experimental data on neutron and gamma-ray fluxes on 21 June, 1980 and 3 June, 1982 requires impulsive phase spectra of accelerated particles, which steepen at high energies (e.g., Bessel-function spectra). Furthermore, to explain the time extended production of neutrons and pions in the 3 June, 1982 flare it is necessary to assume a second phase acceleration process which produces a particle population with extremely hard spectrum. On the contrary our model, by taking into account the configuration of magnetic field at the flare site, naturally leads to a prolonged production of neutrons and pions, and allows us to give an explanation to all available data for these flares within one impulsive acceleration process and one population of primary particles with a power-law energy spectrum up to ~ 1 GeV.

Acknowledgements

We would like to thank S. O. Poroshina for assistance in carrying out some calculations, and A. D. Dudrova, T. S. Myars, V. S. Mutina, and G. V. Selitskaya for help in the preparation of the manuscript.

Appendix I. Inclusive Total and Differential Cross-Sections of Neutron and π^0 Production in $p\alpha$ and $\alpha\alpha$ Interactions

Here we present the cross-sections compiled by Manzhavidze (1987).

Elastic and inelastic cross-sections of the pp and $p\alpha$ reactions, as well as inclusive cross-sections of neutron and π^0 production in the pp-reaction, were measured at different energies and are well known (see, e.g., Lock and Measday, 1970; Meyer, 1972). However, there are no measurements of the neutron and π^0 production inclusive cross-sections in the $p\alpha$ interaction. Murphy, Dermer, and Ramaty (1987) and Hua and Lingenfelter (1987b) estimated the neutron production cross-section based on the cross-sections of the main neutron producing channels of $p\alpha$ collision compiled by Meyer (1972). However, cross-sections presented by Meyer (1972) above 300 MeV were obtained by means of extrapolation from lower energies and were not supported by any experimental data. More recently the $p\alpha$ collision has been studied in the JINR, Dubna

experiment at an energy of 1408 MeV/nucleon (Glagolev *et al.*, 1977, 1980, 1984). The measured cross-sections for some channels differ significantly from Meyer's extrapolations. As a result the inclusive neutron production cross-section is higher than that obtained by Murphy, Dermer, and Ramaty (1987) and Hua and Lingenfelter (1987b) (see Figure 18). The solid curve in that figure is the result of our calculations of internuclear cascade, a program being developed at JINR, Dubna (Barashenkov *et al.*,

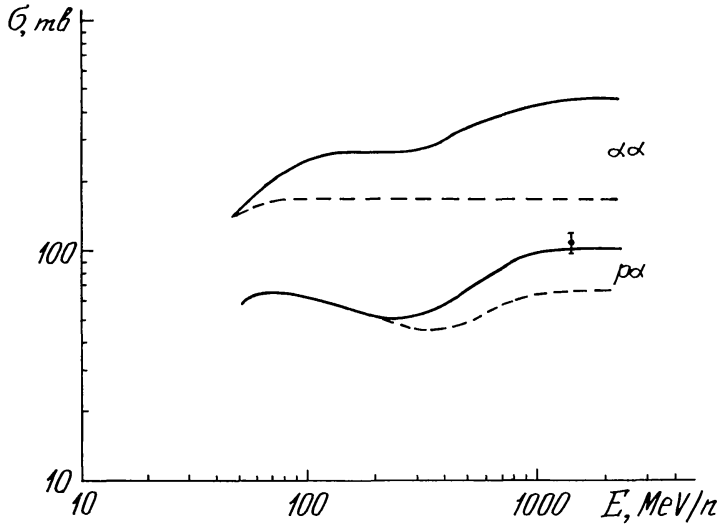

Fig. 18. Inclusive cross-section of neutron production in the $p\alpha$ and $\alpha\alpha$ interaction. Solid lines present our calculations, dashed lines those by Hua and Lingenfelter (1987b). Data point from the JINR, Dubna experiment.

1981; Barashenkov, 1983; Zheregi and Musulmanbekov, 1984). Note the good agreement with the cross-section of Murphy, Dermer, and Ramaty (1987) and Hua and Lingenfelter (1987b) at energies below 300 MeV as well as with the experimental value at 1408 MeV. In the same figure neutron production cross-section in the $\alpha\alpha$ reaction is also given.

In Figure 19 we present inclusive pion production cross-sections in a $p\alpha$ reaction calculated the same way. They are close to those given in Murphy, Dermer, and Ramaty (1987) and also agree with experimental values at 1408 MeV (for charged pions).

We have also applied the program to obtain angular and energy distributions of neutrons and π^0 in $p\alpha$ and $\alpha\alpha$ interactions. As a test we have calculated $\pi^{\pm}$ angular distributions in the laboratory system and compared them to the measured ones. The agreement was good.

The approximations presented below are valid for incident proton energies between 50 MeV and 2 GeV and neutrons with energies greater than 30 MeV.

First let us consider neutrons generated in a $p\alpha$ reaction. The neutron escape angle in the laboratory system is

$$\cos\theta_n = \sum_{i=1}^{6} a_i R^{i-1},$$

where R is the random number uniformly distributed over (0, 1).

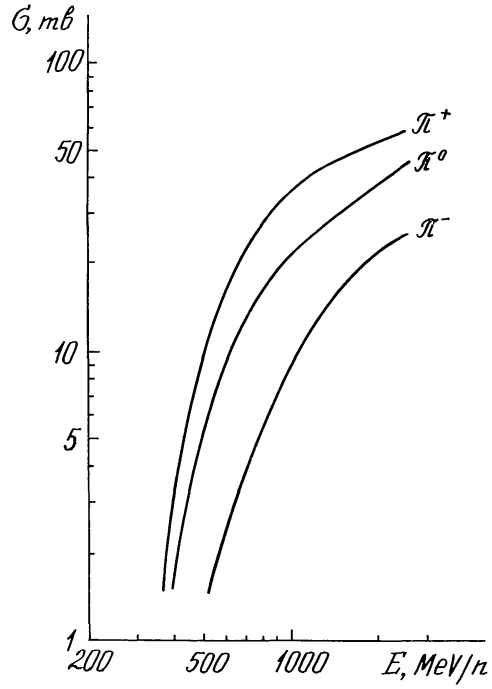

Fig. 19. Inclusive cross-sections of pion production in the $p\alpha$ interaction.

In turn a_i factors are given by polynomials:

$$a_i = \sum_{j=1}^{5} \alpha_{ij} E^{j-1}, \tag{1A}$$

where E is the incident proton energy in the laboratory system (GeV), and α_{ij} are presented in Table II.

TABLE II

α_{ij} coefficients (see relation (1A))

i \ j	1	2	3	4	5
1	−2020(0)[a]	−1214(1)	1470(1)	−7710(0)	1450(0)
2	6776(1)	8172(1)	−4215(1)	−1348(1)	9560(0)
3	−2351(2)	−3806(2)	3288(2)	−6262(1)	−1411(1)
4	4380(2)	8923(2)	−1027(3)	4188(2)	−4082(1)
5	−3906(2)	−9272(2)	1191(3)	−5755(2)	8221(1)
6	1320(2)	3461(2)	−4660(2)	2408(2)	−3837(1)

[a] $-2020(0) = -0.2020 \times 10^0$.

Fixing the obtained value of $\cos\theta_n$ we pass to the neutron energy. The relations are:

$$E_n = T_K \sum_{j=1}^{7} b_{Kj} R^{j-1}, \qquad b_{Kj} = \sum_{i=1}^{5} \beta_{Kji} E^{i-1}, \tag{2A}$$

TABLE III

β_{Kji} coefficients (see relation (2A))

i \ j	1	2	3	4	5
			$K = 1$ $(C < 0)$		
1	−3756(−2)	3574(−1)	−4442(−1)	1998(−1)	−2393(−2)
2	−1401(1)	4296(1)	−5184(1)	2119(1)	−2828(0)
3	2870(2)	−5505(2)	4944(2)	−1077(2)	−6806(0)
4	−1231(3)	1599(3)	−6972(2)	−5008(2)	2420(2)
5	2290(3)	−1560(3)	−1347(3)	2768(3)	−8657(2)
6	−1968(3)	1519(2)	3393(3)	−3948(3)	1103(3)
7	6456(2)	3143(2)	−1786(3)	1765(3)	−4689(2)
			$K = 2$ $(0.0 < C < 0.33)$		
1	1611(−3)	3543(−1)	−4040(−1)	2012(−1)	−3737(−2)
2	5942(0)	−3044(1)	4192(1)	−2527(1)	5389(0)
3	1020(2)	−5122(1)	5075(1)	−2765(0)	−5048(0)
4	−6747(2)	7941(2)	−1038(3)	4757(2)	−6854(1)
5	1606(3)	−2084(3)	2838(3)	−1384(3)	2188(2)
6	−1649(3)	2169(3)	−3015(3)	1488(3)	−2362(2)
7	6191(2)	−7979(2)	1123(3)	−5525(2)	8579(1)
			$K = 3$ $(0.33 < C < 0.67)$		
1	1707(−2)	4430(−1)	−6258(−1)	3692(−1)	−7537(−2)
2	1768(1)	−6537(1)	6509(1)	−2808(1)	4305(0)
3	−2401(1)	2952(2)	−1650(2)	3926(0)	1253(1)
4	−1681(2)	−3444(2)	−5980(2)	7465(2)	−2091(2)
5	6595(2)	−2864(2)	2504(3)	−2227(3)	5624(2)
6	−8161(2)	8525(2)	−3111(3)	2504(3)	−6056(2)
7	3403(2)	−4508(2)	1303(3)	−9970(2)	2352(2)
			$K = 4$ $(0.67 < C < 1.0)$		
1	2861(−1)	−9378(−1)	1429(0)	−8680(−1)	1806(−1)
2	1030(1)	−1028(1)	−7678(0)	1210(1)	−3503(0)
3	9554(1)	−4429(2)	8090(2)	−5285(2)	1139(2)
4	−5220(2)	2810(3)	−5228(3)	3467(3)	−7557(2)
5	1211(3)	−6894(3)	1291(4)	−8599(3)	1879(3)
6	−1297(3)	7568(3)	−1416(4)	9437(3)	−2063(3)
7	5111(2)	−3027(3)	5672(3)	−3783(3)	8277(2)

where K is determined by the above-obtained value of $\cos\theta_n = C$ (see Table III) and T_K is

$$T_K = \sum_{i=1}^{4} \tau_{Ki} E^{i-1}\,; \tag{3A}$$

β_{Kji} and τ_{Ki} are presented in Tables III and IV, respectively. If $E < 0.4$ GeV and $0.67 < \cos\theta_n$, E_n is simply

$$E_n = T_4 R\,.$$

TABLE IV

τ_{Ki} coefficients (see relation (3A))

K \ i	1	2	3	4
1	−0.002	0.549	−0.468	0.135
2	0.023	0.610	−0.451	0.111
3	0.010	0.838	−0.490	0.114
4	−0.059	1.516	−0.799	0.240

For the $p\alpha$ reaction, relations for pion escape angle and its energy in the C-of-M system are (energy in GeV)

$$C = \cos\theta = 2 \sum_{K=1}^{5} a_K R^{K-1},$$

$$a_K = \sum_{i=0}^{5} \alpha_{Ki} E^i, \quad K = 1, 2, 3, 4, \qquad a_5 = 1 - \sum_{K=1}^{4} a_K, \tag{4A}$$

$$E_{\pi^0} = T_K \sum_{j=1}^{4} b_{Kj} R^j,$$

$$b_{Kj} = \sum_{i=0}^{6} \beta_{Kji} E^i, \quad j = 1, 2, 3, \qquad b_{K4} = 1 - \sum_{j=1}^{3} b_{Kj}, \tag{5A}$$

$$T_K = \sum_{i=0}^{3} \tau_{Ki} E^i, \tag{6A}$$

where the factors α_{Ki}, β_{Kji}, and τ_{Ki} are presented in Tables V, VI, and VII, respectively. The incident proton energy is assumed to be greater than 0.35 GeV. Below that level pion production can be considered isotropic.

The relations for neutron angle and energy in the C-of-M system for the $\alpha\alpha$ reaction are:

$$C = \pm \sum_{i=1}^{4} a_i R^{i-1}, \qquad a_i = \sum_{j=1}^{5} \alpha_{ij} E^{j-1}, \tag{7A}$$

TABLE V

α_{Ki} coefficients (see relation (4A))

K \ i	0	1	2	3	4	5
1	9281(1)	−5095(2)	1095(3)	−1076(3)	4922(2)	−8522(1)
2	−3878(2)	2601(3)	−5913(3)	5987(3)	−2783(3)	4861(2)
3	8722(2)	−6123(3)	1414(4)	−1426(4)	6556(3)	−1131(3)
4	−7933(2)	5776(3)	−1332(4)	1318(4)	−5908(3)	9899(2)

TABLE VI

β_{Kji} coefficients (see relation (5A))

j \ i	0	1	2	3	4	5	6
			$K = 1$ $(-1.0 < C < -0.5)$				
1	−6265(1)	3872(2)	−8777(2)	1117(3)	−8170(2)	3138(2)	−4839(1)
2	3864(2)	−2272(3)	5426(3)	−6912(3)	4883(3)	−1781(3)	2599(2)
3	−7056(2)	4147(3)	−9871(3)	1227(4)	−8384(3)	2953(3)	−4168(2)
			$K = 2$ $(-0.5 < C < 0.0)$				
1	−2445(2)	1674(3)	−4392(3)	5874(3)	−4209(3)	1531(3)	−2214(2)
2	8107(2)	−5111(3)	1311(4)	−1746(4)	1258(4)	−4621(3)	6748(2)
3	−1663(3)	1016(4)	−2521(4)	3215(4)	−2215(4)	7802(3)	−1097(3)
			$K = 3$ $(0.0 < C < 0.5)$				
1	−2675(2)	1671(3)	−3876(3)	4503(3)	−2780(3)	8676(2)	−1073(2)
2	1564(3)	−9534(3)	2243(4)	−2641(4)	1650(4)	−5212(3)	6529(2)
3	−2434(3)	1460(4)	−3411(4)	3980(4)	−2458(4)	7643(3)	−9394(2)
			$K = 4$ $(0.5 < C < 1.0)$				
1	2318(2)	−1654(3)	4799(3)	−6745(3)	4896(3)	−1765(3)	2497(2)
2	−1412(3)	1008(4)	−2829(4)	3919(4)	−2832(4)	1022(4)	−1452(3)
3	1855(3)	−1348(4)	3828(4)	−5367(4)	3921(4)	−1427(4)	2041(3)

TABLE VII

τ_{Ki} coefficients (see relation (6A))

K \ i	0	1	2	3
1	−0.166	0.822	−0.538	0.118
2	−0.169	0.784	−0.398	0.064
3	−0.204	0.917	−0.512	0.109
4	−0.303	1.327	−0.870	0.239

$$E_n = T_K \sum_{i=1}^{8} b_i R^{i-1}, \tag{8A}$$

$$T_K = \sum_{i=1}^{4} \tau_{Ki} E^{i-1}. \tag{9A}$$

α_{ij}, b_i, and τ_{Ki} are presented in Tables VIII, IX, and X, respectively.

Pion generation in the $\alpha\alpha$ reaction may be omitted as negligibly small ($\lesssim 1\%$) compared to pp and $p\alpha$ collisions (Ramaty, Kozlovsky, and Lingenfelter, 1975).

TABLE VIII

α_{ij} coefficients (see relation (7A))

i \ j	1	2	3	4	5
1	7590(−3)	−6297(−1)	1201(0)	−8685(−1)	1978(−1)
2	1179(1)	4833(1)	−6301(1)	3756(1)	−7870(0)
3	−2903(−1)	−6067(1)	6352(1)	−3489(1)	7076(0)
4	−1494(0)	1211(1)	−1305(−1)	−2838(0)	8220(−1)

TABLE IX

b_i coefficients (see relation (8A))

i	$E < 0.150$	$0.150 < E < 0.900$	$0.900 < E < 2.000$
1	−1190(−1)	−5300(−2)	−3400(−2)
2	2277(1)	1919(1)	1770(1)
3	−2659(2)	−1707(2)	−1745(2)
4	1669(3)	1005(3)	1025(3)
5	−5147(3)	−3005(3)	−3036(3)
6	8172(3)	4707(3)	4741(3)
7	−6418(3)	−3685(3)	−3713(3)
8	1975(3)	1139(3)	1150(3)

TABLE X

τ_{Ki} coefficients (see relation (9A))

K \ i	1	2	3	4	
1	0.056	0.529	−0.271	0.067	$0 < \lvert C\rvert < 0.25$
2	0.063	0.500	−0.223	0.052	$0.25 < \lvert C\rvert < 0.5$
3	0.042	0.707	−0.460	0.132	$0.5 < \lvert C\rvert < 0.75$
4	0.014	0.839	−0.292	0.041	$0.75 < \lvert C\rvert < 1$

Finally it should be noted that the obtained angular distributions are far from isotropic and energy spectra are quite different in different directions and significantly deviate from the uniform distributions up to the maximal possible value.

Appendix II. Monte Carlo Simulation Technique

The description of the Monte Carlo simulation procedure has been discussed in Kocharov, Mandzhavidze, and Gueglenko (1986, 1987) and Mandzhavidze (1987). Here we present a brief review and add the discussion of pitch-angle scattering simulation technique.

We start by assigning each particle an initial pitch-angle at the top of the loop, $\mu_0 = \cos\vartheta_0 = R$ (isotropic distribution), and energy $E_0 = E_{th}/R^G$ according to the

power-law spectrum. Here $G = (1 - S_p)^{-1}$, S_p is the power-law index, E_0 is the kinetic energy per nucleon, R is a random number uniformly distributed over (0, 1). E_{th} is the threshold energy for high-energy neutron ($E_n > 50$ MeV) or pion production (50 MeV nucl^{-1} or 180 MeV nucl^{-1}, respectively).

As primary particles of species 'i' (protons or α-particles) move inside the loop they lose the energy due to the ionization losses and are removed by nuclear interactions. The probability of nuclear interaction, while particles are decelerated from energy E_1 to E_2, is

$$P(E_1, E_2) = 1 - \exp\left[- \int_{E_2}^{E_1} \frac{\eta_H \left(\sigma_{ip}^{tot} + \frac{n_{He}}{n_H} \sigma_{i\alpha}^{tot} \right)}{|dE/d\kappa|} dE \right],$$

where n_i is a number density of species 'i', $dE/d\kappa$ (MeV nucl^{-1} g^{-1} cm^2) is the ionization loss rate (Nemetz and Gofmann, 1975), η_H is number of protons per gram of the matter, and σ_{ip}^{tot} ($\sigma_{i\alpha}^{tot}$) is total cross-section of the $ip(i\alpha)$ interaction. The primary particle energy at the moment of interaction E_{int} may be obtained from the equation

$$R = 1 - P(E_0, E_{int})/P(E_0, E_{th}) .$$

We propose that each incident particle produces a neutron (or π^0). In this case, to the secondary particle the weight W must be ascribed,

$$W = P(E_0, E_{th}) \frac{\sigma_{ip}^{n(\pi^0)}(E_{int}) + \frac{n_{He}}{n_H} \sigma_{i\alpha}^{n(\pi^0)}(E_{int})}{\sigma_{ip}^{tot}(E_{int}) + \frac{n_{He}}{n_H} \sigma_{i\alpha}^{tot}(E_{int})},$$

where $\sigma_{ip}^{n(\pi^0)}$ and $\sigma_{i\alpha}^{n(\pi^0)}$ are the inclusive cross-sections for neutron (or π^0) production in ip and $i\alpha$ interactions. Similarly, the certain weight is ascribed to every kind of interaction (ip or $i\alpha$). Then we can calculate the column density traversed by the particle till the interaction:

$$\kappa = \int_{E_{int}}^{E_0} dE/|dE/d\kappa| .$$

In the absence of pitch-angle scattering, primary particle motion was studied in detail in Section 2 of Paper I. Using the relations therein one can obtain the pitch angle, the time and the site of nuclear interaction corresponding to the value of κ. Then the angle and the energy of secondaries are determined according to the distributions given in Appendix I.

Treating the propagation of secondary particles we consider elastic and inelastic nuclear collisions of neutrons with ambient hydrogen and Compton scattering and pair production processes for π^0 decay gamma-rays (Mandzhavidze, 1987). Our treatment

is quite similar to that carried out in the previous investigations (e.g., Hua and Lingenfelter, 1987b).

Considering the process of pitch-angle diffusion, we assume that scattering occurs in the coronal part of the loop. In the chromosphere scattering by turbulence generated by external sources was omitted because of the fast damping of MHD waves there. If the evolution of the angular dependence of distribution function f is described by the right-hand side of Equation (2) with the constant ν (Equation (6)), the value of $\langle\mu\rangle = \int_{-1}^{1} \mu f(\mu)\, d\mu$ changes with the rate: $d\langle\mu\rangle/dt = -2\nu\langle\mu\rangle$. This relation may be obtained by integration of Equation (2) over μ. In the same way one can obtain the rate of dispersion $D = \langle\mu^2\rangle - \langle\mu\rangle^2$. Suggesting f to be a sharp function maximal at $\mu = \mu_0$, $dD/dt \approx 2\nu(1 - \mu_0^2)$. This was the reason to simulate the scattering of accelerated particles using the normal distribution with those values of $d\langle\mu\rangle/dt$ and dD/dt (Palmer and Jokipii, 1981). It is proposed that under the initial condition $f(t = 0) \sim \delta(\mu - \mu_0)$ and under $2\nu(1 - \mu_0^2)t \ll 1$ the solution of Equation (2) is close to the Gaussian function. We have verified this proposition. Under the parameters used, the discrepancy was less than or about 10% in the $2\sqrt{D}$-interval near μ_0. Thus we have modelled the process of pitch-angle diffusion by means of many discrete small angle scatterings with the mean path between two scatterings being l. The particle pitch-angle cosine is changed in the following way: $\mu_2 = \mu_1 + (\Delta\mu)_1 + (\Delta\mu)_2$, where μ_1 and μ_2 are pitch-angle cosines before and after scattering, $(\Delta\mu)_1 = -\mu_1(\Delta\mu)_0^2$, $(\Delta\mu)_0^2 = 2\nu(t_2 - t_1)$, and $(\Delta\mu)_2$ is chosen from the Gaussian distribution with standard deviation $\sqrt{(\Delta\mu)_0^2(1 - \mu_*^2)}$, $\mu_* = \mu_1 + (\Delta\mu)_1$. The choice of the value of $(\Delta\mu)_0$ is quite important. First, it should be smaller than any angular scale of the model (e.g., the loss cone angle) and, second, it should be small enough to provide relaxation of the initial beam distribution to isotropy (the beam distribution was used only as a test). These requirements are satisfied by $(\Delta\mu)_0 = 0.08$, which was kept fixed throughout the calculation. The mean path between two scatterings, l, is determined by the turbulence level and also depends on the particle rigidity: $l = (\Delta\mu)_0^2\sqrt{p}/2\nu_0$ (see Section 3). Between two scatterings the coordinate and the energy of particles may be calculated using relations presented in Section 2 of Paper I.

References

Achterberg, A.: 1981, *Astron. Astrophys.* **98**, 161.

Abramov, V. I. and Kotov, Yu.D.: 1987, *Pis'ma v Astron. J.* **13**, 141.

Alexandrov, A. F., Bogdankevich, L. S., and Rukhadze, A. A.: 1978, *Fundamentals of Plasma Electrodynamics*, Visshaya shkola, Moscow.

Barashenkov, V. S.: 1983, Preprint JINR, Dubna, R2–83–117.

Barashenkov, V. S., Gudima, H. K., and Toneev, V. D.: 1969, *Acta Phys. Polonica* **36**, 415.

Barashenkov, V. S., Zheregie, F. G., Musulmanbekov, G. G., Plushchev, V. A., and Solovieva, Z. I.: 1981, *Nucl. Phys. Soviet* **3**, 1061.

Bespalov, P. A. and Trahtengertz, V. Yu.: 1980, *Voprosy Fiziki Plazmy* **10**, 88.

Bespalov, P. A., Zaitsev, V. V., and Stepanov, A. V.: 1986, *Solar Phys.* **114**, 127.

Bykov, A. M. and Toptyghin, I. N.: 1981, *Izv. AN SSSR, Ser. Fiz.* **45**, 474.

Chupp, E. L., Forrest, D. J., and Ryan, J. M., *et al.*: 1982, *Astrophys. J.* **263**, L95.

Chupp, E. L., Forrest, D. J., and Vestrand, W. T. *et al.*: 1985, *Proc. 19th Int. Cosmic Ray Conf., La Jolla* **4**, 126.

Chupp, E. L., Debrunner, H., and Fluckiger, E. *et al.*: 1987, *Astrophys. J.* **318**, 913.
Cooper, J. F., Reppin, C., and Forrest, D. J. *et al.*: 1985, *Proc. 19th Int. Cosmic Ray Conf., La Jolla* **5**, 474.
Dermer, C. D. and Ramaty, R.: 1986, *Astrophys. J.* **301**, 962.
De Jager, C.: 1987, *Proc. 20th Int. Cosmic Ray Conf., Moscow* **7**, 66.
Evenson, P., Kroeger, R., and Meyer, P.: 1985, *Proc. 19th Int. Cosmic Ray Conf., La Jolla* **4**, 130.
Fedorenko, V. N. and Ostryakov, V. M.: 1987, *Astrophysics* **26**, 285.
Forrest, D. J., Vestrand, W. T., and Chupp, E. L. *et al.*: 1985, *Proc. 19th Int. Cosmic Ray Conf., La Jolla* **4**, 146.
Forrest, D., Vestrand, W., and Chupp, E. *et al.*: 1986, *Adv. Space Res.* **6**, 115.
Ginzburg, V. L. *et al.*: 1984, *Cosmic Ray Astrophysics*, Nauka, Moscow.
Glagolev, V. V. *et al.*: 1977, Preprint, JINR, Dubna, PI-10894.
Glagolev, V. V. *et al.*: 1980, Preprint, JINR, Dubna, 1–80–240.
Glagolev, V. V. *et al.*: 1984, Preprint, JINR, Dubna, 1–84–202.
Hua, X.-M. and Lingenfelter, R. E.: 1987a, *Astrophys. J.* **323**, 779.
Hua, X.-M. and Lingenfelter, R. E.: 1987b, *Solar Phys.* **107**, 351.
Holman, G. D., Ionson, J. A., and Scott, J. S.: 1979, *Astrophys. J.* **228**, 576.
Kocharov, G. E.: 1987, *Soviet Sci. Rev., Ser. E, Astrophys. and Space Phys.*, Harwood Academic Publ., Switzerland.
Kocharov, G. E. and Mandzhavidze, N. Z., 1983, *Pis'ma v Astron. Zh.* **10**, 771.
Kocharov, G. E. and Mandzhavidze, N. Z.: 1984, *Izv. AN SSSR, Ser. Fiz.* **48**, 2212.
Kocharov, G. E., Kocharov, L. G., and Kovaltsov, G. A.: 1981, Preprint, Phys.-Tech. Inst., Leningrad, 744.
Kocharov, G. E., Mandzhavidze, N. Z., and Gueglenko, V. G.: 1986, Preprint, Phys.-Tech. Inst., Leningrad, 1088.
Kocharov, G. E., Mandzhavidze, N. Z., and Gueglenko, V. G.: 1987, Preprint, Phys.-Tech. Inst., Leningrad, 1169.
Kocharov, G. E., Kocharov, L. G., Kovaltsov, G. A., Mandzhavidze, N. Z., and Semukhin, P. E.: 1987, *Proc. 20th Int. Cosmic Ray Conf., Moscow* **3**, 74.
Kocharov, G. E., Kovaltsov, G. A., Kocharov, L. G. *et al.*: 1988, *Izv. AN SSSR, Ser. Fiz.* **52**, 2384.
Kocharov, L. G. and Kovaltsov, G. A.: 1990, *Solar Phys.* **125**, 67.
Kovaltsov, G. A. and Kocharov, L. G.: 1987a, Preprint, Phys.-Tech. Inst., Leningrad, 1180.
Kovaltsov, G. A. and Kocharov, L. G.: 1987b, in *Processes on Surface and Interior of the Sun*, Phys-Tech. Inst., Leningrad, p. 135.
Lingenfelter, R. E. and Ramaty, R.: 1967, in W. Shen (ed.), *High Energy Reaction in Astrophys.*, Benjamin Press, New York, p. 99.
Lingenfelter, R. E. *et al.*: 1965, *J. Geophys. Res.* **70**, 4077.
Lock, W. O. and Measday, D. F.: 1970, *Intermediate Energy Nuclear Physics*, Methuen, London.
Mandzhavidze, N. Z.: 1987, Thesis, Phys.-Tech. Inst., Leningrad.
McDonald, F. B. and Van Hollebeke, M. A. I.: 1985, *Astrophys. J.* **290**, L67.
Meyer, J. P.: 1972, *Astron. Astrophys. Suppl.* **7**, 417.
Murphy, R. J. and Ramaty, R.: 1984, *Adv. Space Res.* **4**, 127.
Murphy, R. J., Dermer, C. D., and Ramaty, R.: 1987, *Astrophys. J. Suppl.* **63**, 721.
Nemetz, O. F. and Gofmann, Yu. F.: 1975, *Handbook on Nuclear Physics*, Naukova Dumka, Kiev.
Palmer, I. D. and Jokipii, J. R.: 1981, *Proc. 17th Int. Cosmic Ray Conf., Paris* **3**, 381.
Prince, T. A. *et al.*: 1983, *Proc. 18th Int. Cosmic Ray Conf., Bangalore* **4**, 79.
Ramaty, R. and Murphy, R. J.: 1984, *Proc. Plasma Astrophys. School and Workshop*, ESA SP-207, p. 83.
Ramaty, R. and Murphy, R. J.: 1987, *Space Sci. Rev.* **45**, 213.
Ramaty, R., Kozlovsky, B., and Lingenfelter, R. E.: 1975, *Space Sci. Rev.* **18**, 341.
Rieger, E., Reppin, C., and Kanbach, G. *et al.*: 1983, *Proc. 18th Int. Cosmic Ray Conf., Bangalore* **10**, 338.
Rieger, E., Forrest, D. J., Bazilevskaya, G. A. *et al.*: 1987, *Proc. 20th Int. Cosmic Ray Conf., Moscow* **3**, 65.
Share, G. H. *et al.*: 1983, *Positron-Electron Pairs in Astrophysics*, American Inst. of Physics, New York, p. 15.
Solar Geophys. Data: 1982, No. 456, Part 1, p. 125.
Toptyghin, I. N.: 1983, *Cosmic Rays in the Interplanetary Magnetic Fields*, Nauka, Moscow.
Vestrand, W. T., Forrest, D. J., Chupp, E. L., Rieger, E., and Share, G. H.: 1987, *Astrophys. J.* **322**, 1010.
Zaitsev, V. V. and Stepanov, A. V.: 1985, *Solar Phys.* **99**, 313.
Zheregi, F. G. and Musulmanbekov, G. G.: 1984, Depon. Publication, JINR, Dubna, B3–10–84–873.